Creation of High Energy Density in Matter with Heavy Ion Beams for Equation of State Studies

Vom Fachbereich Physik der

TECHNISCHEN UNIVERSITÄT DARMSTADT

zur Erlangung des Grades
eines Doktors der Naturwissenschaften
(Dr.rer.nat.)

genehmigte Dissertation von
Anna Kozyreva
aus Sankt-Petersburg

Darmstadt 2003
D17

Referent: Prof. Dr. D.H.H. Hoffmann
Korreferent: Prof. Dr. W. Seelig

Tag der Einreichung: 22.10.2003
Tag der Prüfung: 17.12.2003

Zusammenfassung

Die präzise Messung von Zustandsgleichungen in schwerionenerzeugten extremen Zuständen erfordert geeignete Targetanordnungen, um wohldefinierte Zustände im Material zu erzeugen. Ziel dieser Arbeit ist die Untersuchung der Möglichkeiten, mit dem Schwerionenstrahl des SIS-18 bei der GSI Zustände hoher Energiedichte in Materie zu erzeugen, die für solche genauen Zustandsgleichungsmessungen geeignet sind. Zunächst werden hierzu die Grundlagen der Erzeugung extremer Materiezustände mit Schwerionen zusammengestellt. Aus der Diskussion verschiedener Kühlmechanismen ergibt sich eine gegenüber früheren Arbeiten verbesserte Abschätzung der effektiven Heizzeit, welche die maximal erreichbare Temperatur im Target begrenzt.

Um die numerischen Hilfsmittel zu überprüfen, die zur Berechnung neuer Targetkonfigurationen benötigt werden, wurde die Energiedeposition des Ionenstrahls experimentell untersucht. Einen aussagekräftigen Test der hydrodynamischen Rechnungen bietet eine zeitaufgelöste, zweidimensionale Schlierentechnik. Zur Interpretation der experimentellen Daten und um die Verbindung zu den Ergebnissen der Hydrosimulationen herzustellen, wurde ein '3D-Raytracing' Programm entwickelt. Insgesamt ergab sich eine Übereinstimmung der berechneten und experimentellen Schlierenbilder und es konnte gezeigt werden, dass die Schlierentechnik in der Lage ist, Phasengrenzen im Target nachzuweisen. Unterschiede zwischen den experimentellen Ergebnissen und der Hydrosimulation konnten mit der unzureichenden Zustandsgleichung in Zusammenhang gebracht werden, die der Hydrorechnung zugrunde lag. Weiterhin wurde gezeigt, dass für Targetmaterialien mit einer hohen Fließgrenze für die gegenwärtigen Ionenstrahlparameter eine hydrodynamische Beschreibung nicht anwendbar ist. Unter diesen Umständen ist der bestimmende Energiediffusionsprozess die Wärmeleitung. Mit der Schlierentechnik war es möglich, die Ausbreitung einer Wärmewelle im Target zu verfolgen und daraus die Temperatur in der Depositionszone zu bestimmen. Irreversible Veränderungen im Targetmaterial ermöglichen eine zweite, unabhängige Bestimmung der Temperatur im bestrahlten Targetbereich.

Die erhaltenen Ergebnisse zeigen, dass die experimentellen Bedingungen hinreichend genau kontrolliert werden können und dass die numerischen Hilfsmittel präzise genug sind, um fortgeschrittene Targets für Zustandsgleichungsmessungen zu entwickeln. Eine weitverbreitete Methode zur Zustandsgleichungsmessung beruht auf dem Einsatz von Schockwellen, wobei eine ebene Schockwellengeometrie unverzichtbar ist. Diese ergibt sich gewöhnlich nicht in schwerionengetriebenen Schockwellen. Daher wurde eine neue Targetkonfiguration erarbeitet, die ebene Schockwellen erzeugt. Dabei übersteigt der Druck den Druck in einem einfachen Target um ein mehrfaches. Die einzigartige Eigenschaft von Schwerionen, ausgedehnte Materievolumen homogen zu heizen, lässt sich voll nutzen, wenn die Materie isochor geheizt wird. Um den hydrodynamischen Fluss des Targets während der Bestrahlung zu unterdrücken, wird ein dynamischer Einschluss vorgeschlagen. Dieses Konzept ermöglicht homogene Heizung großer Volumen mit einem Einschluss aus Material niedriger Ordnungszahl und ermöglicht damit, Röntgenstreuung mit Hilfe des PHELIX Lasers zur Diagnostik einzusetzen. Die isochore Targetheizung großer Targetvolumen mit Schwerionen, kombiniert mit umfassenden Diagnostikmöglichkeiten, verspricht einen aussichtsreichen Zugang zur Untersuchung von Materie, die als 'warm dense matter' bezeichnet wird.

Abstract

Precise equations of state (EOS) measurements of matter under extreme conditions driven by heavy ion beams require proper target configurations to create well defined states of the studied material. The aim of this work is to evaluate the potential of the SIS-18 heavy ion beam at GSI to produce samples of matter at high energy density suitable for accurate EOS measurements. First the basic principles of matter under extreme conditions driven by heavy ion beams are summarized. The influence of different cooling mechanisms is discussed resulting in an estimation of the effective heating time, which limits the maximum target temperature. This estimation is an improvement compared to previous works.

The energy deposition of ion beams was studied experimentally to evaluate numerical tools which are needed for new target calculations. A time resolved two-dimensional schlieren technique was applied to provide a comprehensive test for hydrodynamic calculations. To interpret the experimental data and to link them to the results of a hydro simulation, a 3D ray-tracing modeling was developed. An overall agreement between computed and experimental schlieren images was found and it was shown that the schlieren diagnostics is capable to detect phase boundaries in the target. Discrepancies between experimental results and the hydro calculation could be connected to an insufficient equation of state that was used for the simulation. It was also demonstrated that for target materials with a high yield point a hydrodynamic description is not applicable for the current beam parameters. Under these circumstances the dominant energy diffusion mechanism is heat conduction. With the schlieren technique it was possible to follow a thermal wave propagating in a target and thus to determine the temperature in the heated zone. Irreversible changes in the target material provide a second, independent way to determine the temperature in the irradiated region.

The obtained results show that the experimental conditions can be well controlled and that the numerical tools are sufficiently precise to develop advanced targets for EOS measurements. A common methods for EOS measurements are shock wave experiments, which demand planar shock wave geometry. That is usually not provided in an ion-beam driven shock. A novel target configuration is proposed to generate a planar shock front with a pressure exceeding the pressure in a bulk sample by several times. The beneficial property of heavy ions to heat extended volumes of matter with good uniformity can be fully utilized, when isochoric heating conditions are fulfilled. To suppress hydrodynamic motion during the ion beam irradiation, a dynamic confinement is proposed. This concept provides homogeneous target heating by a low-Z tamper, which allows to apply x-ray scattering diagnostics using the PHELIX laser at GSI. Isochoric heating of macroscopic samples of matter with heavy ion beams together with excellent diagnostics possibilities promises to become a fruitful approach to warm dense matter studies.

Contents

Chapter 1

Introduction

The equation of state (EOS) describes a physical system by the relation between its thermodynamic quantities, such as pressure, energy, density, entropy, specific heat, etc., and is related to both fundamental physics and applied science. The modern age of EOS research started with P.W. Bridgman (1906–1954), who received the Nobel Prize in 1946 for high pressure physics. The study of the EOS under extreme conditions is an interdisciplinary subject with important applications to material science, astrophysics, geophysics, plasma physics and inertial fusion research. In geophysics the EOS is necessary for understanding the structure of our planet and other planets. In astrophysics the EOS is an integral part of the description of stellar evolution of white dwarfs, supernovae and neutron stars. The knowledge of the EOS in the warm dense matter (WDM) regime is of large importance in inertial fusion research, since the fusion target is crossing the WDM regime at the beginning of the heating and compression phase. In general, for any system which is described by a 'fluid model' the knowledge of the EOS is required to solve the equations of motion.

To obtain an EOS point, three thermodynamic variables, for example density, pressure and internal energy, have to be determined independently with time and space resolution. It is a challenge to perform such measurements in an arbitrarily loaded medium. In case of a planar shock wave, use of the Hugoniot equation reduces the measurements to two quantities. If the matter is heated isochorically, and the energy deposition of a driver is known, the measurement of only one thermodynamic quantity provides a point for the EOS.

The EOS in the high pressure regime is studied experimentally in the laboratory by using static and dynamic techniques. In static experiments the sample is squeezed between pistons or anvils and the pressure and temperature are limited by the strength of the construction materials to a few megabars and a few hundred degrees Celsius [Mao94]. In dynamic experiments shock waves are created. By measuring the shock wave parameters,

such as shock wave speed and particle flow velocity, the EOS is studied. Shock waves can be used to study the EOS for any pressure that can be supplied by a driver, since the disassembly of the target material is always slower than the shock velocity. Chemical explosives have been used to create shock waves up to about 10 Mbars in metals with accompanying temperatures in the order of 10^4 K. Up to 100 Mbars can be reached in underground nuclear tests [Rag84]. Recent laser-driven and pulsed-power-driven compression experiments provided new and unexpected data on the EOS of hydrogen and its isotopes at pressures > 1 Mbar [Len00]. Other shock wave generators are also used, such as two-stage light gas guns, rail guns, and magnetic compression devices.

Gesellschaft für Schwerionenforschung (GSI) Darmstadt provides unique possibilities to create high energy density in matter with intense heavy ion beams. Energetic heavy ions deposit their energy along a straight trajectory with good uniformity over an extended volume. The energy deposition of heavy ions in matter is described by the Bragg curve, which is well known for almost all materials. High currents of heavy ions can be easily transported and focused on a target. All this makes intense heavy ion beams an excellent tool for EOS studies. The construction of a new heavy ion synchrotron facility is currently planned at GSI [Gut01]. After completion, short intense pulses of energetic heavy ions will be able to provide, for instance in solid hydrogen, an energy deposition of up to 1 MJ/g, even higher values can be obtained at the end of the ion range.

The purpose of this work is to assess the potential of the existing SIS-18 synchrotron for EOS measurements of matter at high energy density. The heavy ion beams delivered by the SIS-18 machine have a limited number of ions and a pulse length comparable to the hydrodynamic target response time. To perform precise EOS measurements, special target configurations adapted to the ion beam parameters are necessary. The high-energy, high-power PHELIX laser which is currently installed at GSI can serve as a powerful diagnostics of ion beam heated targets.

The first chapter of this work summarizes the fundamentals of high energy density in matter driven by heavy ion beams. The principles of shock compression, isentropic expansion, and discontinuity decay are discussed. The basics of heavy ion energy deposition in cold matter are considered, following the estimation of the energy relaxation time. Further, an evaluation of different cooling mechanisms in ion beam heated matter is given. The last section of this chapter is dedicated to some special aspects of the equations of state of condensed matter.

An experimental study of ion beam heated matter is reported in chapter two. The aim of the experiment was to check the validity of a hydrodynamic description of the target response and to test the available hydrocode. Ion beam parameters and target materials are chosen such that the experimen-

tal data allow clear interpretation. The applied schlieren technique which was used previously to probe ion beam heated matter [Con02],[Dew03], is enhanced by improving image quality and time resolution. A further step in advancing the schlieren method is made by developing a ray-tracing modeling of the schlieren images. Analysis and interpretation of the experimental results, their comparison with the computed schlieren images and validation of the available numerical technique close this chapter.

Chapter three describes novel target configurations for the EOS measurements with the SIS-18 machine. A tapered tube target is proposed, which allows to create a planar shock with a pressure which is several times higher than that in a bulk sample. The next section of this chapter is dedicated to isochoric heating of targets with heavy ion beams. Here, a new dynamic confinement concept for ion beam heated targets is proposed which provides diagnostic possibilities using the PHELIX laser.

The results of the performed experiments, developed numerical modeling for the schlieren diagnostics, and the proposed target configurations will support future activities in ion beam driven high energy density in matter studies.

Chapter 2

Fundamentals of high energy density in matter driven by heavy ion beams

2.1 Dynamics of matter at high energy densities

Extreme conditions of matter imply high values of state variables, such as high energy density, high temperatures and pressures, and super–sonic velocities. Such extreme conditions become available for experimental investigations with the help of intense beams of energetic particles, high explosives, high-power pulsed lasers, and other sources of high dynamic pressure.

Behavior of matter under conditions of intense dynamic loading are usually examined in the hydrodynamic approximation, since the pressure developed in a solid body is much higher than its yield point, whose typical value at room temperature is several kbar. The elastoplastic properties of the medium become significant as the load pulse applied to the material decreases. In the regime of high pressures, when large density changes occur, the equations of gas-dynamics are appropriate because they take into account compressibility of matter in contrary to the hydrodynamic equations for incompressible fluids.

The state of the moving gas with known thermodynamic properties can be defined in terms of its velocity, density and pressure as functions of coordinate and time. If we neglect the contributions of relaxation processes, namely viscosity and thermal conductivity, the motion of a compressible medium is described by a set of partial differential equations expressing the laws of conservation of mass, momentum and energy, supplemented by the equation

of state:

$$\frac{d\rho}{dt} + \rho \,\mathrm{div}\mathbf{u} = 0, \quad \rho\frac{d\mathbf{u}}{dt} = -\nabla p, \quad \frac{d\epsilon}{dt} + p\frac{dV}{dt} = Q, \quad \epsilon = \epsilon(p,\rho)\,, \tag{2.1}$$

where $\mathbf{u}$ is the mass velocity of matter, ϵ is its internal energy density, $V = 1/\rho$ is the specific volume, and Q is the energy generated by the external sources. The equation of state (EOS) $\epsilon = \epsilon(p,\rho)$ defines the thermodynamic properties of matter. This equation is a property of the matter itself, and every material has its own unique description.

The propagation of an ordinary sound or acoustic wave in matter is accompanied by low amplitude longitudinal displacements of molecules. There is no net flow of matter, and any physical changes in the material are small and reversible. Therefore a small change in pressure is related to a small change in density by the isentropic derivative, $\Delta p = (\partial p/\partial\rho)_S \Delta\rho$. This derivative represents the square of the local sound speed

$$c^2 = \left(\frac{\partial p}{\partial \rho}\right)_S = \frac{V}{\kappa} \tag{2.2}$$

and refers to the undisturbed matter; $\kappa = -(1/V)(\partial V/\partial p)_s$ is the isentropic compressibility.

A different situation arises when a disturbance is driven through matter at a speed greater than the local sound speed. Since the molecules can only move away from the supersonic disturbance at the sound speed, a compression wave with very steep gradients of pressure, density, and temperature is formed. Such a wave is called a shock wave and it is an irreversible process due to its suddenness.

In the basic theory of shock waves, heat transport and viscosity are neglected and flow variables are discontinuous between the undisturbed and the shocked regions. For an idealized planar shock conservation laws for mass, momentum, and energy result with respect to the stationary reference frame in the following relations

$$\rho_0 D = \rho_1(D-u_1),\ p_1 - p_0 = \rho_0 D u_1,\ p_1 u_1 = \frac{1}{2}(\rho_0 D u_1^2) + \rho_0 D(\epsilon_1 - \epsilon_0), \tag{2.3}$$

where D is the velocity of the front; indices 0 and 1 represent an initial, unshocked state and a final state, as the shock wave has passed by, respectively. These equations can be combined to eliminate the velocities, yielding the Rankine-Hugoniot equation for internal energy jump in terms of pressures and specific volumes

$$\epsilon_1 - \epsilon_0 = \frac{1}{2}(V_0 - V_1)(p_1 + p_0). \tag{2.4}$$

Including the equation of state with the three jump conditions results in four equations with five variables: p, V, ϵ, D and u. Thus, there is only one

independent variable, and a curve is defined in a five-dimensional variable space. This is called the "Rankine-Hugoniot curve". In reality, there is a family of Hugoniots for a given material, each centered on an initial state defined by p_0 and V_0. The $p-V$ Hugoniot is not a path that is followed during compression or any special thermodynamic path, but rather the location of all possible end states that can be achieved behind a single shock wave passing through a material at a given initial state.

A shock wave is supported in the material if the sound speed is an increasing function of pressure. It is that property that causes a compression wave to steepen into a shock (see e.g. [Lan02]):

$$\left(\frac{\partial^2 V}{\partial p^2}\right)_s > 0. \tag{2.5}$$

Stability criteria require a shock wave to be subsonic with respect to the shocked state, so that a disturbance trailing the shock would be able to catch up:

$$c_1 + u_1 \geq D. \tag{2.6}$$

A small compressive disturbance ahead of the shock wave must be moving slower than the shock front:

$$D > c_0. \tag{2.7}$$

Dissipative mechanisms, such as viscosity and heat transport, prevent the shock from becoming a true, infinitesimally thin discontinuity. In reality, the velocity gradient can only increase until viscous stress becomes important. The temperature gradient is similarly limited by thermal transport mechanisms. When these dissipative forces become significant, they begin to cancel the effect of increasing sound speed with pressure which is the driving force behind the steepening compression wave. This means that entropy is generated by the conversion of mechanical energy to heat. Therefore the process is adiabatic, since there is no heat exchange between the system and the surroundings, but it is non-isentropic, and thus irreversible.

The ability of a material to generate pressure under given loading conditions is defined by the shock impedance

$$Z \equiv \rho_0 D\,, \tag{2.8}$$

which is generally a function of pressure. For materials that have Hugoniots that are everywhere upwardly concave in the $P - V$ plane, it is clear that the shock impedance increases with increasing shock pressure. In the limit of weak shocks, when $D \sim c$, the impedance is considered to be independent of pressure. The material is described by the constant acoustic impedance.

Rarefaction, or release, waves are the mechanism by which a material returns to ambient pressure. Thus the direction of wave propagation is opposite to the direction of the pressure gradient. In most of the materials

the sound speed increases with pressure. This property causes the rarefactions to spread out as they propagate. In contrast to shocks, rarefactions do not usually involve significant energy dissipation, so they can be regarded as reversible, or isentropic, processes.

Intense pulse loading of matter creates a discontinuity in either pressure or particle velocity that cannot be sustained in any material. If a discontinuity in either of these variables is created at some point by impact or wave interaction, the resulting motion will be such that the pressure and particle velocity become continuous across the point of interaction. The motion will consist of one or more waves propagating away from the point of the discontinuity. Other variables, such as density, can be discontinuous without giving rise to wave motion. Such a discontinuity is known as a "contact discontinuity".

There are two typical cases of discontinuity decay: when two shock waves propagate in both directions from the point of discontinuity, and when a shock wave propagates in one direction and a rarefaction wave in another. The corresponding pressure profiles and phase trajectories on the $p-u$ plane are shown in Fig. 2.1 and 2.2. In the first case, initial discontinuity in a particle velocity u_0 results in two shock waves. The material behind these shock waves has the same pressure p_1 and particle velocity u_1. In the second case, the pressure discontinuity decays into a rarefaction wave propagating in the medium having initially high pressure p_0, and a shock wave running in the opposite direction. Compression and rarefaction waves formed as a result of the decay of discontinuity transforms the medium to a state with the same pressure p_1 and particle velocity u_1, so that the final state simultaneously satisfies both phase trajectories for these two waves.

There is a special type of hydrodynamic motion, in which all the flow variables do not depend on the coordinate and time independently, but are functions only of the combination x/t. This decreases the number of independent variables by one, therefore the flow is described by ordinary rather than by partial differential equations. The distributions of all quantities with respect to the x coordinate change with time without changing their form. This type of motion is isentropic and called self-similar. It occurs when gasdynamic equations and also the relations describing the thermodynamic properties of the fluid do not contain any characteristic length and time scale. If dissipative processes are neglected, there is only one dimensional parameter of fluid, the speed of sound. Thus, if the boundary and initial conditions do not contain any characteristic length or time scales, the flow can depend on the coordinate and time only in the combination x/t, which has the dimension of a velocity.

As an example of self-similar motion, we consider planar unsteady flow of gas into vacuum. Let the gas initially have constant parameters and occupy a half space $x > 0$. At the time $t = 0$ the gas starts to flow into vacuum, and a

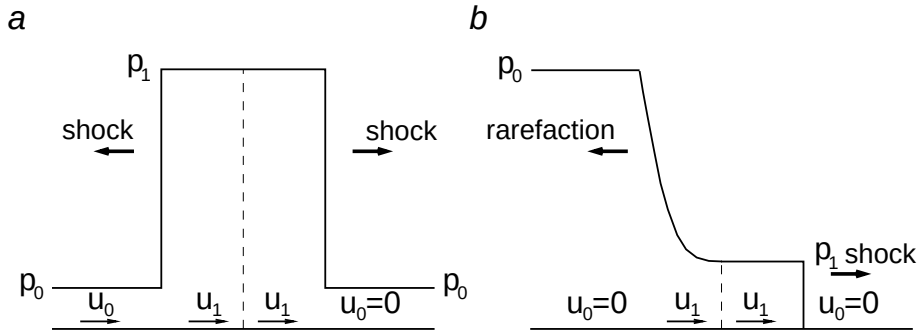

Figure 2.1: Pressure profiles for two cases of discontinuity decay: a – initially the medium on the left of the broken line has velocity u_0; on the right of the line, the medium is at rest; b – initially the medium on the left of the broken line is at pressure p_0, whereas on the right, $p = 0$. Arrows at the bottom show the direction of motion of the medium; bold arrows show the direction of wave propagation.

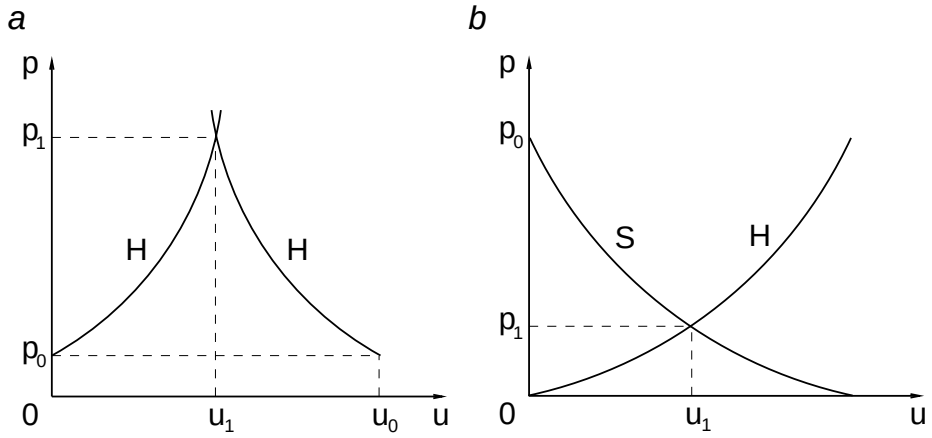

Figure 2.2: Pressure vs. mass velocity diagram for the two cases of discontinuity decay of Fig. 1.1. H – shock Hugoniots; S – release isentrope.

rarefaction wave starts running through the undisturbed gas. It is possible to find an exact analytic solution to this problem, if a perfect gas with constant specific heat is assumed [Zel67]. The gas expands until its density, pressure and temperature (speed of sound) reach zero, and its boundary moves to the left with the velocity

$$u_{\max} = \frac{2}{\gamma - 1} c_0. \tag{2.9}$$

The velocity and density profiles for planar expansion of gas into vacuum are shown in Fig. 2.3.

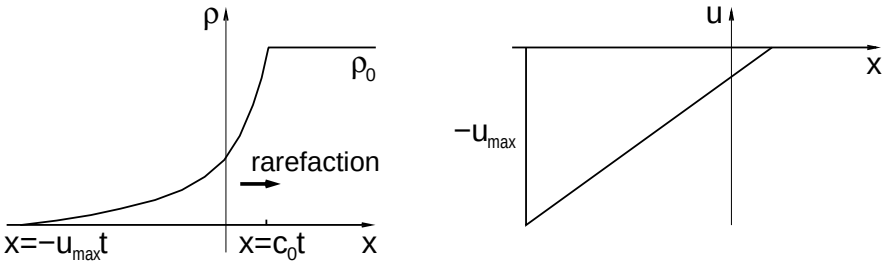

Figure 2.3: Density and velocity profiles in plane unsteady gas flow into vacuum.

If the gas occupies initially a cylindrical volume of radius R_0, the flow is isentropic, but not self-similar. The problem contains a characteristic length scale: the initial radius of the gas cloud. This impedes analytical solution of the problem.

At $t = 0$ the gas starts to expand into vacuum, and a rarefaction wave starts running inward. It approaches the cylinder axis and a reflected rarefaction wave starts to move outward. It can be shown that during the isentropic expansion the disturbances originating in the interior regions of the cloud do not reach the boundary [Sta60]. Hence this surface moves with the constant velocity $u_{\max}$. The relationship governing the motion of the boundary of the cloud is $R = [2/(\gamma-1)]c_0 t + R_0$. It is not possible to find an exact analytical solution to this problem, since the flow is not self-similar.

This problem has the property that the flow asymptotically approaches a self-similar one with time. The role of the initial length parameter R_0 becomes less important during the later highly expanded stage where $R \gg R_0$. The thermal part of the energy approaches zero during the expansion and, consequently, the kinetic energy approaches the total energy of the gas E. The equation of motion for the limits $t \to \infty$ and $R \to \infty$ takes the asymptotic form

$$\frac{du}{dt} = \frac{\partial u}{\partial t} + u\frac{\partial u}{\partial r} \to 0, \tag{2.10}$$

that is, the velocities of the fluid particles approach constant value and $u = r/t$.

The average, root mean square, velocity of gas asymptotically approaches the constant limiting value $u_\infty = \sqrt{(2E/M)}$ (M is the total mass of the gas, E is the total energy), which is related to the boundary velocity as

$$u_{\max} = \sqrt{\frac{2\gamma}{\gamma-1}}u_\infty. \tag{2.11}$$

Substituting the asymptotic solution for the velocity $u = r/t$ into the continuity equation, and taking into account that $R = u_{\max}t$, one sees that

it is satisfied by the density function

$$\rho = \frac{f(r/R)}{R^2}, \tag{2.12}$$

where f is a completely arbitrary function of r/R. The asymptotic distribution of the density with respect to the radius does not change with time. It changes in the same ratio as R increases, remaining similar to itself. In the absence of any forces acting on the gas, each particle will move with a constant inertial velocity, there will be no redistribution of mass, and the density profile will remain unchanged. The density distribution is formed in an earlier stage, when the pressure forces are acting on the gas.

2.2 Energy deposition of heavy ions in cold matter

At Gesellschaft für Schwerionenforschung, Darmstadt, intense beams of energetic heavy ions are applied to create matter at high energy densities. In this section, stopping of heavy charged particles in cold, non-ionized matter is discussed.

The projectile interacts with the medium via the Coulomb force with the electrons and protons and via the strong nuclear force with the nuclei of the absorber. At the ion energy below 1 GeV/u, that is used for high-energy-density physics applications, nuclear force can be disregarded[1]. The projectile slows down by losing energy to the atoms of the absorbing medium.

A fast ion incident on matter collides with the target electrons and with the target nuclei. The first process is called electronic stopping or inelastic energy loss, the latter nuclear stopping or elastic energy loss. The electrons take an appreciable amount of energy from the heavy projectile without causing significant deflection. The nuclei absorb very little energy but due to their greater charge cause scattering of the incident particle. Thus energy loss of the projectile occurs in collisions with the target electrons. Sometimes electrons are detached from the atom, sometimes the atom is excited but not ionized. In the following consideration no distinction is made between the two processes, they are simply called excitation. The scattering is confined to rather small angles, so that a heavy ion keeps a straight trajectory while losing energy until it is near to the end of its range.

To calculate the rate of energy loss by a particle of charge $Z_p e$ as it progresses through a medium containing N_e electrons per cm^3, we first consider the electrons to be free and at rest. The force between the heavy particle

[1]Kinetic energy of a projectile per atomic mass unit is $E_{\rm kin} = \frac{M_p}{A_p} c^2(\gamma - 1)$, or $9.32 \cdot 10^8 \cdot (\gamma - 1)\,$eV; $E_{\rm kin} = 1\,$GeV/u corresponds to $\gamma \simeq 2$.

and the electron is $Z_p e^2/r^2$, where r is the distance between them. We can consider the collision to take place in such a short time that the electron acquires a momentum without changing its position during the collision. This is called fast passage approximation. Thus, the momentum acquired by the electron must be perpendicular to the trajectory of the heavy particle and can be calculated by

$$\triangle p = \int_{-\infty}^{\infty} eE_\perp \, dt = \int eE_\perp \, \frac{dx}{v_p} = |Z_p|e^2 \int_{-\infty}^{\infty} \frac{1}{r^2} cos\theta \, \frac{dx}{v_p} = \frac{2|Z_p|e^2}{bv_p} \,, \quad (2.13)$$

where $E_\perp$ is the component of the electric field at the position of the electron normal to the trajectory of the particle (Fig. 2.4) and v_p is the velocity of the heavy particle, which is taken to be constant during the collision.

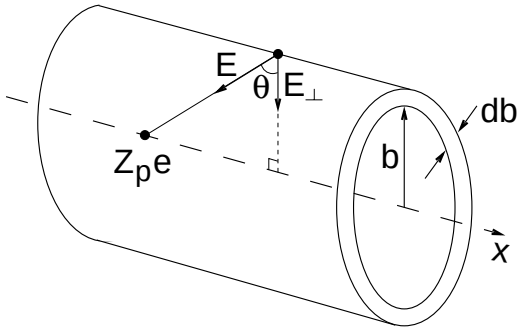

Figure 2.4: Transfer of momentum to an electron by a moving heavy charge.

The energy transferred to the electron is then

$$\frac{(\triangle p)^2}{2m_e} = \frac{2}{m_e} \left(\frac{Z_p e^2}{bv_p} \right)^2 \quad (2.14)$$

and since there are $2\pi N_e b \, db \, dx$ electrons per length dx that have a distance between b and $b + db$ from the heavy ion, the electron energy loss per path length dx is

$$\begin{aligned} S_e = -\frac{dE}{dx} &= 2\pi N_e \int b \, db \frac{(\triangle p)^2}{2m_e} = 4\pi N_e \frac{Z_p^2 e^4}{m_e v_p^2} \int_{b_{\min}}^{b_{\max}} \frac{db}{b} \\ &= 4\pi N_e \frac{Z_p^2 e^4}{m_e v_p^2} \ln \frac{b_{\max}}{b_{\min}} \,. \end{aligned} \quad (2.15)$$

This is the stopping power of the absorbing medium. The last factor in (2.15) is the so-called Coulomb logarithm. The integral cannot be extended from zero to infinity. It would be incompatible with the conditions under which

Eq. (2.14) was derived; for instance, distant collisions last a long time, and the corresponding energy transfer is not given by this equation.

In reality the electrons are not free but are bound in atomic orbits. As long as the collision time, b/v_p, is short compared to the orbital period of motion, the collision will be sudden enough to treat the electron as free. The condition $b/v_p < \tau = 1/\bar{\omega}$ must be fulfilled, where $\bar{\omega}$ is an appropriate average of the frequencies of the atom. The limit for $b_{\max}$ then becomes

$$b_{\max} = v_p/\bar{\omega}. \tag{2.16}$$

The equation (2.14) was derived under the assumption that the electron does not move substantially during the collision. As long as the distance the electron actually moves is small compared to b, the equation for energy transfer will be correct. The distance traveled by the electron during the collision is of the order of

$$d \sim \frac{\triangle p}{2m} \times \triangle t = \frac{|Z_p|e^2}{mv_p^2} = b_{\min}\,. \tag{2.17}$$

As long as $b \gg d$, (2.14) should hold.

Introducing in Eq. (2.15) the values of $b_{\max}$ and $b_{\min}$ one obtains the classical formula for energy loss of a non-relativistic charged particle, how it is given in [Jac75],

$$S_e = -\frac{dE}{dx} = \frac{4\pi Z_p^2 e^4}{m_e v_p^2} N_e \ln \frac{m_e v_p^3}{|Z_p|e^2\bar{\omega}}\,. \tag{2.18}$$

The quantity $\hbar\bar{\omega} = I$ is a special average of the ionization potentials in the atom of the stopping material. Expression (2.18) shows that the stopping power is proportional to $1/v_p^2$ and has a maximum at the end of the range where v_p drops to zero; this maximum is called Bragg peak.

Bohr [Boh15] has established a semi-classical theory of the energy loss of fast charged particles caused by their inelastic collisions with atoms. In this approach collisions are classified according to their impact parameter. Close collisions are considered to be interactions of the projectile with free electrons, which follow classically well-defined trajectories. Distant collisions are treated as classical energy transfer to a charged harmonic oscillator in a spatially uniform electric field due to the passing particle. Bohr has obtained the following result for the energy loss of relativistic ions

$$S_{e_{Bohr}} = -\frac{dE}{dx} = \frac{4\pi Z_p^2 e^4}{m_e v_p^2} N_e \left[\ln \frac{1.123 m_e v_p^3}{|Z_p|e^2\bar{\omega}(1-\beta^2)} - \frac{\beta^2}{2}\right]. \tag{2.19}$$

Bethe [Bet30] has solved the problem quantum mechanically in the first Born approximation. This formulation classifies the collisions according

to their momentum transfer. Close collisions are as well considered to be the interactions of projectile with free electrons. Therefore, the effect of atomic binding is disregarded. Distant collisions, with low momentum transfer, are treated as first-order dipole excitation. By imposing this approach, Fano [Fan63] has obtained the relativistic Bethe formula

$$S_{e_{Bethe}} = -\frac{dE}{dx} = \frac{4\pi Z_p^2 e^4}{m_e v_p^2} N_e \left[\ln \frac{2m_e v_p^2}{\hbar\bar{\omega}(1-\beta^2)} - \beta^2 \right] . \tag{2.20}$$

The Bethe formula is valid only if $|Z_p|\alpha/\beta \ll 1$, or $\hbar v_p \gg e^2|Z_p|$. This corresponds to the regime of validity of the first Born approximation which is the limiting case of a very small perturbation compared to the unperturbed energies and forces[2]. The opposite limit, $|Z_p|\alpha/\beta \gg 1$, is the limit of very strong interactions and corresponds to the regime of validity of Bohr's results. For heavy ions Bohr's approach is working. In the intermediate region, in which the classical and quantum-mechanical formulae complement one another, Bloch solution is valid [Ahl80]. $|Z_p|\alpha/\beta$ can be thought of as the ratio of the classical size of the scattering center, $Z_p e^2/(mv_p^2)$ ($\triangle p = 2mv_p$ – the largest change of the momentum of an electron in (2.13)), to the de Broglie wavelength of the scattered electron. Figure 2.5 shows the energy loss of $1\,\mathrm{GeV/u}$ ^{238}U ion in solid hydrogen obtained with the help of the computer program SRIM [Zie01].

The instantaneous projectile charge, Z_p, is an important quantity in the stopping mechanism. An extensive review on heavy-ion charge states was given by Betz [Betz83]. It is necessary to distinguish between the average equilibrium charge and the effective charge. The average equilibrium charge, $\bar{Z}$, is defined as the actual charge of the particle inside the target. The effective charge, $\bar{Z}_{\mathrm{eff}}$, is calculated from the measured values of the stopping power:

$$S(Z_0, v_p) = \bar{Z}_{\mathrm{eff}}^2(v_p) S(1, v_p) , \tag{2.21}$$

where Z_0 is the nuclear charge of the projectile, $S(1, v_p)$ is the energy loss of protons. The effective charge, $\bar{Z}_{\mathrm{eff}}$, determines the difference between the energy loss of heavy ions and protons at the same velocity. The ratio of ion effective charge to Z_0 is empirically known and depends in good approximation only on the ion velocity. The definition (2.21) of the effective charge is based on the Bethe formula, where the charge of the projectile should be considered to be equal to the effective charge

$$Z_p = \bar{Z}_{\mathrm{eff}} . \tag{2.22}$$

In the regime where Bohr's results are valid ($\hbar v_p \ll e^2|\bar{Z}| \approx e^2|Z_{\mathrm{eff}}|$), this definition of the effective charge is not suitable, since the Coulomb logarithm

[2] $\alpha = e^2/(\hbar c) = 1/137.036$ is the fine structure constant

in the stopping formula includes the average equilibrium charge:

$$\ln \frac{1.123 m_e v_p^3}{|\bar{Z}| e^2 \bar{\omega} (1-\beta^2)} \,. \tag{2.23}$$

The validity of the above formulae relies on the assumption that the speed of the incident particle is much greater than that of the electrons bound to the absorbing medium. Semi-empirical corrections were found in order to modify the stopping formula for energetic inner-shell atomic electrons [Bic72]. For solids, the Bohr-Bethe-Bloch formulae are valid if the projectile velocity exceeds $3v_f$, where v_f is the Fermi velocity of the absorbing material (v_f is about equal to the Bohr velocity v_0). This corresponds to an ion energy of about 200 keV/u.

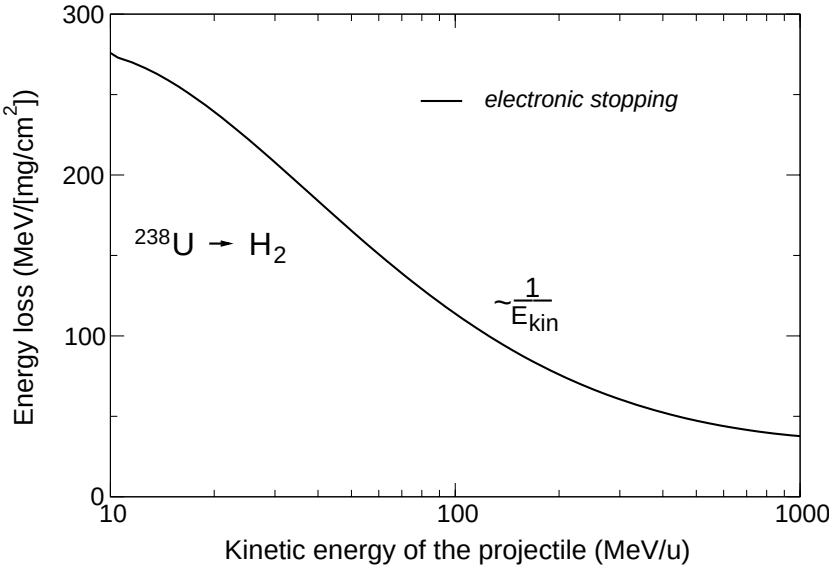

Figure 2.5: Energy loss of 1 GeV/u ^{238}U ions in solid hydrogen. The data are taken from the computer code SRIM [Zie01].

At the end of the range, where the projectile velocity is less than the Fermi velocity of a solid, the majority of target electrons move much faster than the ion. This regime corresponds to projectile energies less than 30 keV/u. Lindhard and Scharff [Lin61] used a model of a slow heavy ion in a uniform free electron gas to calculate low velocity stopping. The electrons have a slight drift velocity relative to the ion. During a collision with the ion, a net energy is transferred which is proportional to this velocity, so that the stopping power shows behavior like a classical friction force: $S_e = -dE/dx \sim v_p$. At the region between low and high ion velocity, $v_f < v_p < 3v_f$, a smooth interpolation has to be used to approximate energy loss.

As ions slow down in matter, atomic electrons become attached to the ions until they become fully neutralized, at which point elastic nuclear collisions, i.e. deflections in the screened electric field of the atom, become the dominant energy-loss process. A detailed description of the energy loss of the moderate velocity ions can be found in [Zie85].

If the target material is ionized, for free electrons $\bar{\omega}$ in the Bohr-Bethe-Bloch formulae has to be replaced by the plasma frequency $\omega_p = \sqrt{\frac{4\pi N_e e^2}{m_e}}$ [Lar59]. It is always true that $\omega_p < \bar{\omega}$, so the stopping power of a plasma is higher than that of cold matter. This is because energy is transferred more easily to free electrons than to bound electrons. Energy loss of swift heavy ions in plasma was extensively measured at GSI [Die92],[Hof94],[Rot00].

2.3 Relaxation processes in matter heated by heavy ions

It was shown in the previous section that fast heavy charged particles slowing down in matter transfer most of their energy to the target electrons. To calculate the hydrodynamic response of ion beam heated matter, one has to know over which distances and times electron energy will be thermalized.

The number of electrons per unit length with transferred energy E in the interval dE is obtained from (2.14)

$$dN(E) = 2\pi N_e \, b \, db = \frac{2\pi (Z_p e^2)^2 N_e}{m_e v_p^2} \cdot \frac{dE}{E^2} \,. \tag{2.24}$$

The energy spectrum of the excited electrons sharply decreases like E^{-2} with energy, so that most of the ion beam energy is deposited into low energy electrons. Following [Arn88], the average energy is estimated as

$$E_{\mathrm{av}} = \frac{\int E \, dN(E)}{\int dN(E)} \cong E_{\mathrm{min}} \ln \left(\frac{E_{\mathrm{max}}}{E_{\mathrm{min}}} \right) \,, \tag{2.25}$$

where $E_{\mathrm{max}} = 2 m_e v_p$ is the maximum energy transferred in a central collision and E_{min} is the minimum energy transferable to the target electrons which is the average ionization potential I for bound electrons (for plasma it is the plasmon energy $\hbar\omega_p$). From this, the average energy of primarily excited electrons is of the order of 10–100 eV.

The Coulomb cross section of an electron at energy E with another electron is

$$\sigma(E) = \pi \left(\frac{e^2}{E} \right)^2 \ln \Lambda \gtrsim \pi \left(\frac{e^2}{E} \right)^2 \,, \tag{2.26}$$

where $\ln\Lambda$ is the Coulomb logarithm [Ros65]. In our case $\ln\Lambda \lesssim 5$. The electron mean free path is therefore

$$l_{ee} = \frac{1}{N_e\sigma} \cong \frac{E^2}{\pi e^4 N_e}\,, \tag{2.27}$$

and the electron-electron collision time

$$\tau_{ee} = \frac{l_{ee}}{v_e} \cong \frac{m_e^{1/2}E^{3/2}}{\pi e^4 N_e}\,. \tag{2.28}$$

For electrons with $E < 100\,\mathrm{eV}$ and $N_e > 10^{20}\,\mathrm{cm}^{-3}$, one obtains $l_{ee} < 10\,\mu\mathrm{m}$ and $\tau_{ee} < 1\,\mathrm{ps}$. Whereas energy relaxation in electron-electron collisions occurs typically in a single collision, the energy transfer between electrons and ions is much slower because of the large difference in mass: $\tau_{ie} = (m_i/m_e)\tau_{ee}$. For protons, the thermalization between electrons and ions will occur in less than 1 ns for the near solid densities considered here. Therefore, in the hydrodynamic calculations it can be assumed that the deposited ion beam energy is thermalized locally and instantaneously.

2.4 Energy balance in ion beam heated matter

In the investigation of dense matter heated with heavy ion beams, local and immediate thermalization of the deposited energy can be assumed, as it was shown above. In this section, the ratio between heavy ion beam heating and cooling mechanisms, such as hydrodynamic motion, heat conduction, and thermal radiation, will be analyzed to determine the thermodynamic state of the target matter that can be reached. In the following, initially solid targets will be mainly discussed.

The specific internal energy, ϵ, will follow the general energy balance equation (2.1). In Lagrangian coordinates, when a given fluid particle is determined in time, the partial derivative with respect to the time $\partial/\partial t$ is equivalent to the total derivative $\mathrm{d}/\mathrm{d}t$, and the energy conservation equation can be written as

$$\frac{\partial\epsilon}{\partial t} = -p\frac{\partial V}{\partial t} - W_{\mathrm{el}} - W_{\mathrm{rad}} + P_{\mathrm{s}} \tag{2.29}$$

where $p\partial V/\partial t$ is the hydrodynamic work term, W_{el} and W_{rad} are the energy losses due to heat conduction and radiation per unit mass of the material per unit time, P_{s} is the specific power deposited by the ion beam.

Initially, the specific internal energy will rise with the heating term P_{s}. The final temperature can be obtained by inverting the equation of state $\epsilon = (\rho, T)$, since P_{s} is given. The increase of the temperature will slow down

or even stop, when the heated volume starts to expand. For solid targets at temperatures in the 1 eV range and in the hydrodynamic regime, heat conduction and thermal radiation are negligible. Therefore, the temperature increase is limited by the hydrodynamic cooling term. The ratio between the specific power deposition and focal spot size of the ion beam defines the time which is needed for the rarefaction wave to propagate over the whole target volume. In case of the SIS-18, the ion beam pulse will be longer, than so defined effective heating time.

2.4.1 Hydrodynamic expansion

To perform analytical estimates and corresponding numerical calculations of the hydrodynamic response of ion beam heated matter, parameters foreseen for the SIS-18 machine at GSI are taken [Spi99]. 2×10^{11} uranium ions of 200 MeV/u delivered in a 100 ns flat top pulse and focused down to $r_\mathrm{b} = 350\,\mu$m (spot radius) deposit – for example in solid hydrogen – $P_\mathrm{s} = 6.3\,\mathrm{TW/g}$ of specific power. A rectangular radial profile of the beam current density is assumed.

Heavy ion beams deposit their energy with a good uniformity over an extended volume. If the target can be made long enough, and expansion waves from the ends do not approach the investigated volume, the target hydrodynamics can be reduced to a one-dimensional problem.

An analytical equation of state of the ion beam heated matter can be written as [Bas85]

$$p = p(\rho, \epsilon) = c_0^2(\rho - \rho_0) + \Gamma\rho\epsilon \tag{2.30}$$

where c_0 is the initial sound speed, ρ_0 is the initial density, and Γ is the Grüneisen parameter of the material (see section 2.5). From this the sound speed at $\rho = \rho_0$ is

$$c = \left(\frac{\partial p}{\partial \rho}\right)_S^{1/2}\Bigg|_{\rho=\rho_0} = \left(c_0^2 + \Gamma\left(\Gamma+1\right)\epsilon\right)^{1/2} . \tag{2.31}$$

Consider a cylindrical target of radius $R_0 = r_\mathrm{b}$, heated with an ion beam of given specific power deposition P_s. The specific internal energy will initially rise with time as $\epsilon = P_\mathrm{s} \cdot t$. A rarefaction wave, propagating with the sound speed into the heated volume, arrives at the center of the target at time t_H. From

$$R_0 = \int_0^{t_\mathrm{H}} \left(c_0^2 + \Gamma\left(\Gamma+1\right)P_\mathrm{s}t\right)^{1/2}\,dt \tag{2.32}$$

one obtains effective heating time

$$t_\mathrm{H} = \frac{\left(\frac{3}{2}R_0\Gamma\left(\Gamma+1\right)P_\mathrm{s} + c_0^3\right)^{2/3} - c_0^2}{\Gamma\left(\Gamma+1\right)P_\mathrm{s}} . \tag{2.33}$$

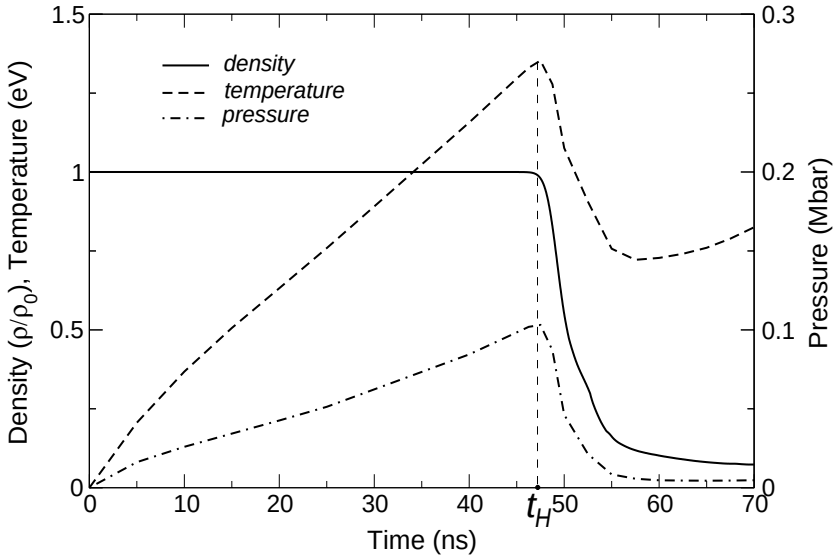

Figure 2.6: Evolution of density, temperature and pressure on the axis of a solid hydrogen cylinder heated uniformly with the ion beam. Power deposition is $P_\mathrm{s} = 6.3\,\mathrm{TW/g}$.

Assuming $c_0^2 \ll \Gamma\,(\Gamma+1)\,\epsilon$ and $\Gamma\,(\Gamma+1) = 1$, one gets $t_\mathrm{H} = (9R_0^2/4P_\mathrm{s})^{1/3}$, how it was obtained in [Arn88]. When $t > t_\mathrm{H}$, internal energy is converted into kinetic energy in the whole heated volume. The maximum specific internal energy can be estimated as

$$\epsilon_\mathrm{max} \cong P_\mathrm{s} \cdot t_\mathrm{H}\,. \tag{2.34}$$

For solid hydrogen irradiated with the SIS-18 beam ($P_\mathrm{s} = 6.3\,\mathrm{TW/g}$) the effective heating time is $t_\mathrm{H} = 34\,\mathrm{ns}$ ($c_0 = 2.1 \cdot 10^5\,\mathrm{cm/sec}$, Γ=2/3). Fig. 2.6 shows the results of 1-D hydrodynamic simulations for the taken beam-target configuration using the SESAME equation of state [SES83]. Density, temperature, and pressure at the target axis are plotted as a function of time. According to the simulations, the heating time is $t_\mathrm{H} = 47\,\mathrm{ns}$. The analytical formula for t_H gives a lower value because the equation of state (2.30) assumes a continuous increase of pressure with internal energy, and, for hydrogen, does not account for dissociation of the molecules.

In the above consideration, a rectangular radial profile of the beam current density was assumed. More realistic is a Gaussian radial distribution of the beam current density. In this realistic case the definition of the heating time is incorrect. Since the second spatial derivative of the Gaussian profile is not zero in the vicinity of the target axis, the hydrodynamic expansion of matter near the axis will start from the very beginning of the beam heating. Detailed numerical calculations are necessary in this case.

2.4.2 Thermal radiation

In general, radiative transfer and radiant heat exchange have an influence on the state of matter. This influence is caused by the fact that the matter loses or gains energy by emitting or absorbing radiation. Hence, the state of matter can be described by the hydrodynamic equations which must be generalized to include the interaction between radiation and matter. Since the radiative transfer is also a function of the state of matter, a system of equations describing matter and radiation consists of a generalized set of hydrodynamic equations together with a radiative transfer equation.

At sufficiently low temperatures, however, the state of matter is practically independent of radiation, and the problem of determining the radiation field and the state of matter can be treated separately. The state of matter is described by hydrodynamic equations, while the radiation field may then be found from the known density and temperature distributions and the known absorption coefficients. Hence, for ion beam heated targets, we are not interested in determining the entire radiation field in the medium (since it does not affect the state of the medium), but we are interested in determining the radiation emitted from the surface of the heated volume.

Depending on the dimensions of the heated volume compared to the photon mean path, the photons born deep within the sample will escape the heated volume or will be absorbed during transit. The heated medium is characterized by the spectral mass absorption coefficient (opacity), $\varkappa_\nu$, which is a function of density and temperature. When radiation at each point of a medium with a nonuniform temperature is close to equilibrium, then the medium is in local thermodynamic equilibrium (LTE) between radiation and matter. If a local temperature (and thus LTE) is defined, an effect of the induced emission can be taken into account through the Boltzmann equation. The reduced spectral mass absorption coefficient has a form: $\varkappa_\nu^{'} = \varkappa_\nu \left(1 - e^{-\frac{h\nu}{kT}}\right)$. The optical thickness of the sample is defined as $\tau_\nu^{'} = \varkappa_\nu^{'} \rho r$, where ρ is density, and r is the radius of the heated cylinder. Radiation passing through a unit optical thickness is attenuated by a factor of e. The value, $l_\nu^{'} = 1/\varkappa_\nu^{'}\rho$ is the radiation mean path. Since we are not primarily interested in the problem of the spectral distribution of the radiation, an appropriately defined mean value of the absorption coefficient is used. The manner in which the mean value is calculated depends on the characteristics of the problem under consideration.

Optically thin target. If $\tau_\nu^{'} \ll 1$, the sample is optically thin and emits as a volume radiator. Only a fraction of the order of $r/l_\nu^{'} \ll 1$ of the photons born at any point of the sample are absorbed during their transition. The radiation intensity of the sample is considerably lower than the equilibrium radiation intensity (the radiation is strongly out of equilibrium with the matter).

In case of an optically thin target the energy lost by the matter turns out

to be equal (with an accuracy of the order of $r/l_\nu^{'}$) to the emitted energy (see e.g. [Zel67]):

$$W_{\rm rad} = \varkappa_{\rm p} U_{\rm p} c\,,\ \varkappa_{\rm p} = \frac{\int_0^\infty \varkappa_\nu^{'} U_{\nu{\rm p}}\, d\nu}{\int_0^\infty U_{\nu{\rm p}}\, d\nu} = \frac{15}{\pi^4}\int_0^\infty \varkappa_\nu^{'} \frac{u^3}{e^u - 1}\, du\,,\ u = \frac{h\nu}{kT}\,, \quad (2.35)$$

where $U_{\nu{\rm p}}$ is the equilibrium radiant spectral energy density function, $U_{\rm p}$ is the frequency integrated equilibrium energy density, $\kappa_{\rm p}$ is the Planck mean opacity (or emission mean). The condition for the validity of the Planck mean as a measure of the emissivity of a thin sample in LTE is $\varkappa_\nu^{'}\rho r \ll 1$ and not $\varkappa_{\rm p}\rho r \ll 1$. This latter condition is not as stringent.

For a hydrogen plasma with density $10^{-4}\,{\rm g/cm^3}$ at a temperature 10 eV under conditions of bremsstrahlung emission, the Planck mean free path is $l_{\rm p} \cong 23\,{\rm cm}$. The mean free path for red light with $\lambda = 650\,{\rm nm}$ is in this case equal to $l_\nu^{'} \cong 1.5\,{\rm mm}$. If the dimensions of the body are much smaller than $l_\nu^{'}$, then the body emits as a volume radiator and the rate of radiative energy loss is $W_{\rm rad} \cong 2\,{\rm TW/g}$. However, this temperature regime is not accessible with the SIS-18 ion beam parameters.

Optically thick target. In the case of an optically thick sample, when $\tau_\nu^{'} \gg 1$, the emitted photons are actually born in the surface layer. Accordingly, the radiation spectrum of an optically thick body is close to the equilibrium spectrum corresponding to the brightness temperature or the surface temperature. Once the assumption of LTE is made, the use of the diffusion approximation is justified when considering radiative transfer. The law for the average of the mean free path with respect to frequency when the radiant heat exchange has the same character as heat conduction is following:

$$l_{\rm R} = \frac{1}{\varkappa_{\rm R}\rho} = \frac{\int_0^\infty l_\nu^{'} \frac{dU_{\nu{\rm p}}}{dT}\, d\nu}{\int_0^\infty \frac{dU_{\nu{\rm p}}}{dT}\, d\nu} = \frac{15}{4\pi^4}\int_0^\infty l_\nu^{'} \frac{u^4 e^{-u}}{(1-e^{-u})^2}\, du\,,\ u = \frac{h\nu}{kT}\,, \quad (2.36)$$

where $\varkappa_{\rm R}$ is the Rosseland mean opacity (or diffusion mean). Note that in contrast to the Planck mean, the Rosseland mean is an inverse mean and thus emphasizes small values of the absorption coefficient. The Planck mean emphasizes large values of the absorption coefficient. As a rule, the different methods in averaging over the spectrum do not lead to large numerical differences between mean free paths; $l_{\rm p}$ and $l_{\rm R}$ usually do not differ by more than a factor of two or four.

In case of the optically thick body, the radiation flux from the surface can be estimated as

$$S \cong l_{\rm R} c \frac{U_{\rm p}}{r}\,. \quad (2.37)$$

The radiant energy loss of an optically thick cylindrical sample is

$$W_{\rm rad} = 2\pi r \frac{\partial S}{\partial m} = \frac{2}{\rho r} S = \frac{2c}{(\rho r)^2 \varkappa_{\rm R}} U_{\rm p}\,, \quad (2.38)$$

where $\partial m = 2\pi r \rho \partial r$ is the increment of the cylindrical Lagrangian mass coordinate.

In calculations of the mean absorption coefficients, it is useful to have limits for the values to be expected for these quantities. Bernstein and Dyson have presented a theorem which places an upper limit on the Rosseland mean opacity (see [Arm72] or [Ims86]). Their result may be given as

$$\varkappa_{\mathrm{R}} \leqslant 4.43 \cdot 10^5 \frac{Z}{A} \left(\frac{\mathrm{Ry}}{kT} \right) . \tag{2.39}$$

In this relation Z is the atomic number, A is the atomic weight, and Ry is the Rydberg number[3]. For relatively low temperatures (of the order of 10 eV) and near solid density, the actual Rosseland opacities are rather close to this limit.

A solid hydrogen cylinder with radius 350 μm heated up to 2 eV, radiates according to this estimation $W_{\mathrm{rad}} \cong 0.1\,\mathrm{MW/g}$, which is much less than the beam deposition power. However, for low density gas targets the energy loss due to the thermal radiation can already be significant at temperatures of about 1 eV, but the opacity calculations are complex in this regime.

2.4.3 Heat conduction

Heavy ion beams release energy within the body, thus a thermal flux transported by heat conduction appears. Heat conduction promotes energy diffusion and temperature equalization. In general, temperature gradients also give rise to pressure gradients, which set the material into motion. In many cases hydrodynamic energy transport dominates over that associated with heat conduction. However, often the motion and hydrodynamic energy transport are unimportant and heat is transported by means of thermal conduction alone. For temperatures which are not to high it is ordinary heat conduction which serves as the mechanism of heat transfer.

Suppose that at the time $t = 0$ energy is released at the center of a sphere. The solution of the problem for linear heat conduction, when the coefficient of thermal diffusivity $\chi \approx const$, is well known. The heat flows in such a manner that the main part of the energy is concentrated in a sphere whose radius is of the order of

$$r \sim \sqrt{4\chi t} . \tag{2.40}$$

The rate of propagation of heat is

$$\frac{dr}{dt} \sim \left(\frac{\chi}{t} \right)^{1/2} \sim \frac{\chi}{r} \sim \frac{r}{t} . \tag{2.41}$$

A model for the heat conduction covering the wide range from the solid state to the high temperature plasma is presented in [Eid00].

[3] $1\mathrm{Ry} = \frac{m_e e^4}{2\hbar^2} = 13.6\,\mathrm{eV} = 2.18 \cdot 10^{-11}\,\mathrm{erg}$.

2.5 Equations of state of condensed matter under extreme conditions

The equation of state is described by a functional relationship between the thermodynamic variables defined for a system in equilibrium. If one neglects the electron-phonon interactions then the thermodynamic functions can be expressed as a superposition of terms. The pressure p and the specific internal energy ϵ of a solid material can be divided into three parts (see e.g.[Eli02]):

$$\epsilon = \epsilon_{\mathrm{c}} + \epsilon_{\mathrm{T}} + \epsilon_{\mathrm{e}}, \quad p = p_{\mathrm{c}} + p_{\mathrm{T}} + p_{\mathrm{e}}\,, \tag{2.42}$$

where ϵ_{c} and p_{c} are the energy and the pressure at zero temperature, ϵ_{T} and p_{T} are the contributions of the thermal motion of the atoms to the energy and the pressure, while ϵ_{e} and p_{e} are the electron thermal contributions.

The first part, the elastic component p_{c} or ϵ_{c}, is related exclusively to the forces of interaction between the atoms (molecules) of the medium and is entirely independent of the temperature. p_{c} and ϵ_{c} depend only on the density of the material and are equal to the total pressure and specific internal energy at absolute zero temperature ("cold" pressure and energy). The state of mechanical equilibrium of a solid at zero temperature and pressure[4] is characterized by the mutual compensation of the interatomic forces of attraction and repulsion and by a minimum in the elastic potential energy, which can be taken as the origin for the energy $\epsilon_{\mathrm{c}} = 0$.

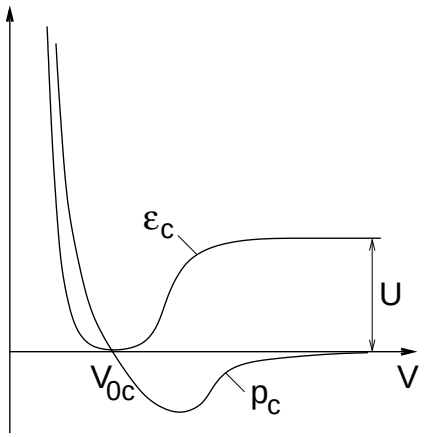

Figure 2.7: Potential energy and elastic pressure curves of a body as a function of the specific volume.

[4]Atmospheric pressure is negligibly small in comparison with the pressures which arise even for very small changes in the volume of the body. Therefore it makes no difference whether the body is in vacuum (p_{c}=0) or at atmospheric pressure ($p_{\mathrm{c}} = 1\,\mathrm{atm}$).

The potential curve and the pressure curve for a body as a function of its specific volume are shown schematically in Fig. 2.7, where V_{0c} denotes the specific volume of a body at zero temperature and pressure. If the volume V is greater than the zero volume V_{0c}, then the attractive forces predominate. The interaction forces fall off rapidly as the distance between the atoms increases. Hence, when the volume increases, the potential energy increases asymptotically to a constant value U equal to the binding energy of the atoms in the body. U is equal to the heat of vaporization at absolute zero. The repulsive forces, which increase sharply with decreasing interatomic distance, dominate when a body is compressed, and thus the potential energy ϵ_c increases rapidly when the volume is less than its zero value.

The elastic pressure is related to the potential energy by

$$p_c = -\frac{d\epsilon_c}{dV}\,. \tag{2.43}$$

The elastic pressure at V_{0c} is zero; the pressure increases rapidly with compression, and becomes negative with expansion. The negative sign of the pressure describes the physical fact that in order to expand the body from the zero volume V_{0c}, a tensile force must be applied. The slope of the cold compression curve determines the speed of sound[5] (at $T = 0$ the isentropic and isothermal compressibility are identical)

$$c_0 = V\left|\frac{\partial p}{\partial V}\right|_S^{1/2}\,. \tag{2.44}$$

The atoms of a material are set into motion by heating. A certain energy and pressure are connected with the thermal motion of the atoms. At temperatures less or equal to 1 eV, the electronic terms are small and can be neglected in (2.42). If the temperature is not too high, the atoms of a solid (or a liquid) undergo small vibrations about their equilibrium positions. The vibrations are harmonic as long as the vibrational energy, that is of $3kT$ per atom, is appreciably less than the height of the potential barrier, ΔU. The height of the barrier in a solid at standard density is of the order of one or several eV. It is somewhat less than the binding energy, usually $\Delta U \approx (0.5 \div 0.7)U$. The compression very sharply increases the repulsive forces between neighboring atoms, and the height of the potential barrier increases rapidly. At sufficiently high temperatures the atoms move freely through the body. The threshold temperature may be defined as $T_k = \frac{2}{3}\frac{\Delta U}{kN}$. When $T \gg T_k$, the thermal energy is the sum of the kinetic energy of translational motion and the potential energy. Fig. 2.8 shows schematically the thermal energy as a function of temperature.

[5]This can be done when the effects connected with the strength of solids and existence of shear strains and stresses are not important.

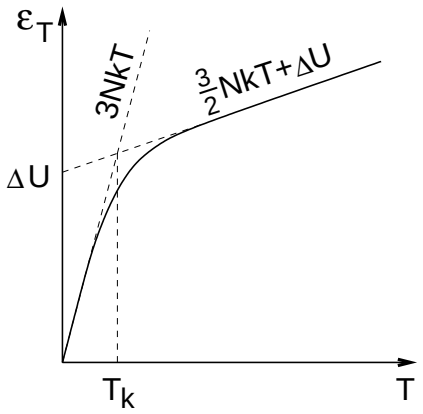

Figure 2.8: Dependence of thermal energy on temperature.

Neglecting the electron excitation, and assuming that the atoms of the body vibrate harmonically about their equilibrium positions, the equation of state and the internal energy of the body can be expressed in the form:

$$\begin{aligned} p &= p_{\mathrm{c}}(V) + p_{\mathrm{T}}(V,T)\,, \\ \epsilon &= \epsilon_{\mathrm{c}}(V) + 3NkT\,, \end{aligned} \tag{2.45}$$

where N is the number of atoms per unit mass. This equation shows, that the thermal pressure is proportional to the temperature, and can be written as[6]

$$p_{\mathrm{T}} = \mathit{\Gamma}(V)\frac{\epsilon_{\mathrm{T}}}{V}\,. \tag{2.46}$$

The quantity $\mathit{\Gamma}$ characterizing the ratio of the thermal pressure to the thermal energy of the lattice is called Grüneisen coefficient.

The Grüneisen coefficient for metals at standard conditions is close to 2. At very high compression and low density the limiting value for $\mathit{\Gamma}$ for all materials is $\frac{2}{3}$. In the SESAME library of equations of state [SES83] the following interpolation formula for compressed matter is used:

$$\mathit{\Gamma}(V) = \frac{\mathit{\Gamma}_0 V}{V_{0\mathrm{c}}} + \frac{2}{3}\left(1 - \frac{V}{V_{0\mathrm{c}}}\right)\,, \tag{2.47}$$

where $\mathit{\Gamma}_0$ corresponds to $V_{0\mathrm{c}}$. It is possible to construct other interpolation formulae to fit experimental data and admit hydrodynamic calculations, see for example [Bus87].

In the derivation of (2.46), it was assumed that the thermal energy is independent of volume. Under this assumption, the Grüneisen coefficient is found to be independent of temperature. However, in the limit of very high

[6]The temperature dependence of the thermal pressure can be obtained from the general thermodynamic identity $\left(\frac{\partial \epsilon}{\partial V}\right)_T = T\left(\frac{\partial p}{\partial T}\right)_V - p$, noting that ϵ_{T} is independent of volume.

temperatures when the thermal motion of the nuclei becomes random, (2.46) should become the equation of state for a monatomic gas, and $\Gamma \to \frac{2}{3}$ as $T \to \infty$.

Chapter 3

Experimental studies of ion beam – matter interaction by means of the schlieren method

At the Gesellschaft für Schwerionenforschung, Darmstadt, intense beams of energetic heavy ions are used to heat extended volumes of condensed media to temperatures of about one eV. Energetic heavy ions penetrate deep into the target volume. The stopping power is described by sophisticated models and is well known for most materials. The effects of energy and angular straggling do not lead to a significant increase of the heated region and can be disregarded. All this makes intense heavy ion beams an appropriate driver for high energy density studies. However, the heavy ion beams available at GSI have considerable pulse duration, so that energy starts to diffuse during the heating time. For moderate temperatures it is heat conduction that serves as the mechanism of energy diffusion. If the temperature within the body is sufficiently high to create pressure gradients that set material into motion, hydrodynamic energy transport will dominate over heat conduction.

The performed experiments are aimed at understanding the phenomena occurring in condensed media by the interaction with intense beams of energetic heavy ions and clarifying the scope of hydrodynamic approximation to describe ion beam heated matter. The targets were made out of transparent media, and the schlieren visualization method was used. The illumination level in a schlieren image responds to the first spatial derivative of the refractive index in the sample.

Schlieren images can be compared to the results of hydrodynamic calculations. This provides an excellent test for the validity of hydro codes. To compute a schlieren image out of flow quantities, the refractive index as a function of density, temperature and wavelength of the diagnostic light has to be known.

3.1 Aim of the experiments

The experiments were intended to clarify the ability of a hydrodynamic approach to describe the response of condensed media to heating with intense beams of energetic heavy ions. To obtain clear and comprehensive information about the irradiated sample, the schlieren diagnostics was chosen. This requires target materials that are transparent in the optical range. Comparisons of computed and experimental schlieren images are ideal tests of the hydrodynamic code and can serve for interpretation of the experimental data [Set01]. It is much easier to judge the overall level of agreement, and therefore to validate the hydrodynamic code, when comparing computed and experimental schlieren images, instead of comparing many individual profile plots of flow quantities.

In order to get clear experimental results, the following features have been considered:

Energy optimization. The range of heavy ions with some hundred MeV is several times larger than the diameter of the deposition zone. Heavy ion beams provided by the SIS-18 synchrotron have a pulse duration of about $0.5\,\mu$s. During the heating time a radial shock starts to propagate, and the range of the ions in the vicinity of the target axis continuously increases (see section 4.1). This effect can be avoided with a low energy beam. The incident ions should have an energy $\lesssim 50\,\mathrm{MeV/u}$.

Material optimization. Water was chosen as a target where a hydrodynamic description is clearly applicable. The decay of discontinuities in a solid body can be accurately examined in hydrodynamic approximation, if the developed pressure is much higher than the yield point of the material. To observe the phenomena induced in a solid body by intense heavy ion beam, targets made out of fused silica have been chosen.

Material	ρ_0, g/cm^3	c_0, km/s	c_l, km/s	σ_T, kbar
Water	0.998	1.48	–	–
Fused silica	2.204	3.77	5.96	72

Table 3.1: Density ρ_0, bulk (c_0) and longitudinal (c_l) sound speed and dynamic yield point σ_T for the target materials.

The table 3.1 contains the parameters of water and quartz at normal conditions. Water, being a fluid, has only one, plastic speed of sound c_0.

Time resolution. For heating of matter with the SIS-18 ion beam the target parameters can be regarded as constant on a time scale of 10 ns. In a schlieren set-up, a pulsed laser with a pulse length of few ns is used as a light source to provide adequate time resolution.

3.2 Principle of schlieren imaging

The schlieren method is used to obtain information about transparent optical phase objects. A phase object is defined as one which alters the phase but not the amplitude of the incident wave. An object of this type is of nonuniform optical thickness, but does not absorb any of the incident light. In the conventional schlieren system, a test object is examined with parallel light. The gradients of the refractive index in the test object lead to the deflection of the beam.

If the gradients of the refractive index are not too large, the approximation of geometrical optics can be used. A differential equation of the light rays which specifies the rays in terms of the refractive index function $n(\vec{r})$ has the form (see for example [Bor02])

$$\frac{d}{ds}\left(n\frac{d\vec{r}}{ds}\right) = \operatorname{grad} n\,, \tag{3.1}$$

where $\vec{r}$ is the position vector of a point on the ray, s is the length of the ray measured from the fixed point on it. The curvature vector of the ray is defined as

$$\vec{K} = \frac{d\vec{s}}{ds} = \frac{1}{\rho}\vec{\nu}\,, \tag{3.2}$$

where $\vec{s}$ is a unit vector in the direction of the normal to the geometrical wave front, $1/\rho$ is the reciprocal of the radius of the curvature, $\vec{\nu}$ is the unit principal normal at a typical point of the ray.

From (3.1) and (3.2) it follows that

$$n\vec{K} = \operatorname{grad} n - \frac{dn}{ds}\vec{s}. \tag{3.3}$$

This relation shows that the gradient of the refractive index lies in the osculating plane of the ray.

Multiplying (3.3) scalarly by $\vec{K}$ and using (3.2) one obtains

$$|\vec{K}| = \frac{1}{\rho} = \vec{\nu}\cdot \operatorname{grad}\, \ln n\,. \tag{3.4}$$

Since ρ is always positive, this implies that as we proceed along the principal normal the refractive index increases, i.e. the ray bends towards the region of higher refractive index. To calculate the deflection angle of the ray, one has to integrate (3.4) along the ray path (see Fig. 3.1)

$$\alpha = \int\limits_s \frac{1}{n}\vec{\nu}\operatorname{grad} n\, ds\,. \tag{3.5}$$

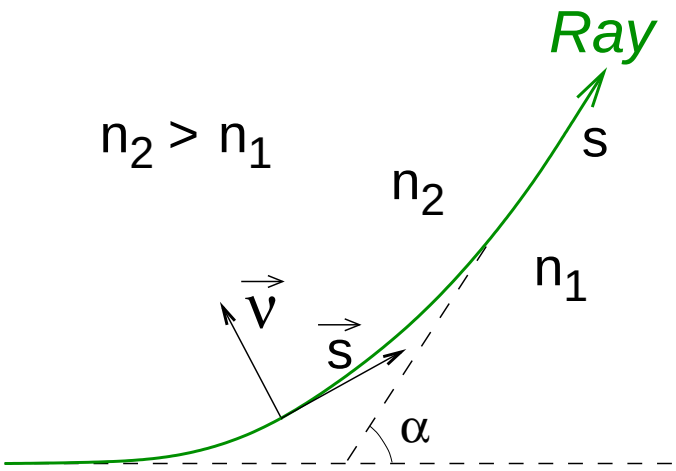

Figure 3.1: Bending a ray in a heterogeneous medium.

A schlieren set-up is an optical system that projects line-of-sight information on refractive index gradients onto an image plane. In the basic arrangement, a parallel light beam traverses the test object and is focused by a lens or spherical mirror, named the schlieren head. An inverted image of the light source is formed in the focal point of the schlieren head. A beam stop is placed in the plane of the light source image to cut off part of the transmitted light. It provides a way to separate the extraordinary light rays — refracted by schlieren in the test area — from the ordinary rays that provide the background illumination. In the symmetric dark field illumination method [Emr81], applied in the performed experiments, a nontransparent circular beam stop is used. The rays deflected in the test object pass the beam stop, and can be detected by the camera. The camera lens is used to focus an inverted image of the schlieren test area on a viewing screen. From the Fourier-optics point of view, the dark field method blocks the zero$^{\text{th}}$ order of the spatial frequency spectrum in the beam stop plane. This produces bright higher-order features against a dark background. Due to the circular beam stop, radial symmetry in all directions perpendicular to the optical axis is achieved.

The schlieren image is an optical image formed by a lens, and thus bearing a conjugate optical relationship to the schlieren object. Even if the studied object is non-planar, an equivalent "object plane" is assumed, in which the ray deflections appear to be located. To compare the results of the hydrodynamic simulations with the experimental schlieren images, post-processing of the calculated flowfield is required. The density and temperature fields extracted from the hydrodynamic simulations are taken to calculate the distribution of the refractive index. A computed schlieren image is obtained by integrating the refractive index gradients along the ray paths and displaying them by amplitude or color using computer graphics.

3.3 Experimental set-up

The heavy ion synchrotron SIS-18 at GSI, Darmstadt is able to provide intense beams of energetic heavy ions suitable for creation of high energy density in matter. In the year 2002, up to 2×10^9 particles of U^{73+} accelerated to 230 MeV/u were delivered to the HHT cave for the experiments. The ion beam consisted of a single pulse with a length of 300 ns (FWHM of a fitted Gaussian profile). The experiment set up for investigation of heavy ion beam – matter interaction by means of the schlieren technique is shown on the Fig. 3.2. The plasma lens was used to focus the beam down to a diameter of less than 1 mm (FWHM). A graphite absorber was placed behind the plasma lens to decrease the energy of the ions. At the target position the incident ions have an energy of 52 MeV/u. Energies of the ions passing through the plasma lens, absorber and air distances are listed in Fig. 3.2. The ion energies were calculated using the ATIMA code based on the LS theory [Lin96], that was developed at GSI to calculate various physical quantities characterizing the slowing-down of protons and heavy ions in matter. According to ATIMA, the energy straggling of the beam as a result of the deceleration is $\Delta E_\mathrm{i} = 0.2\,\mathrm{MeV/u}$.

A Nd:YAG laser (New-wave Minilase I) at 532 nm with an energy of 20 mJ in a 5 ns pulse was used as light source for the schlieren imaging. The laser beam was expanded in two steps to a diameter that can probe the entire ion beam target. The laser beam traverses the target from the side and is then focused onto a beam stop by the schlieren head. The beam stop has a diameter of 0.5 mm, which is much larger than the laser focal spot. The smallest deflection angle which can be measured in such a schlieren system is given by the focal length of the schlieren head and the beam stop diameter:

$$\alpha_\mathrm{min} = \frac{d}{2f_\mathrm{s}} \simeq 0.8\,\mathrm{mrad}. \tag{3.6}$$

The rays whose deflection angles are large than α_min can be detected on the camera. The camera objective projects the apparent position of the object plane onto the CCD chip. To record a schlieren image, a gated camera PCO Dicam PRO was used. Since the time resolution of the schlieren system is set by the 5 ns laser pulse, the exposure time of the camera can be taken sufficiently long to detect the scintillation caused by the ion beam. Note that in the perfectly aligned schlieren set-up, the laser beam axis has to coincide with the line of sight of the camera. Fig. 3.3 shows the timing of ion beam, plasma lens current, camera exposure time and laser trigger for a typical schlieren image. The dashed curve is the Gaussian fit to the actual beam current that was used for numerical simulations. The form of the measured ion current shape is varying from shot to shot. Nevertheless, the Gaussian profile is always a suitable fit of the measured ion current.

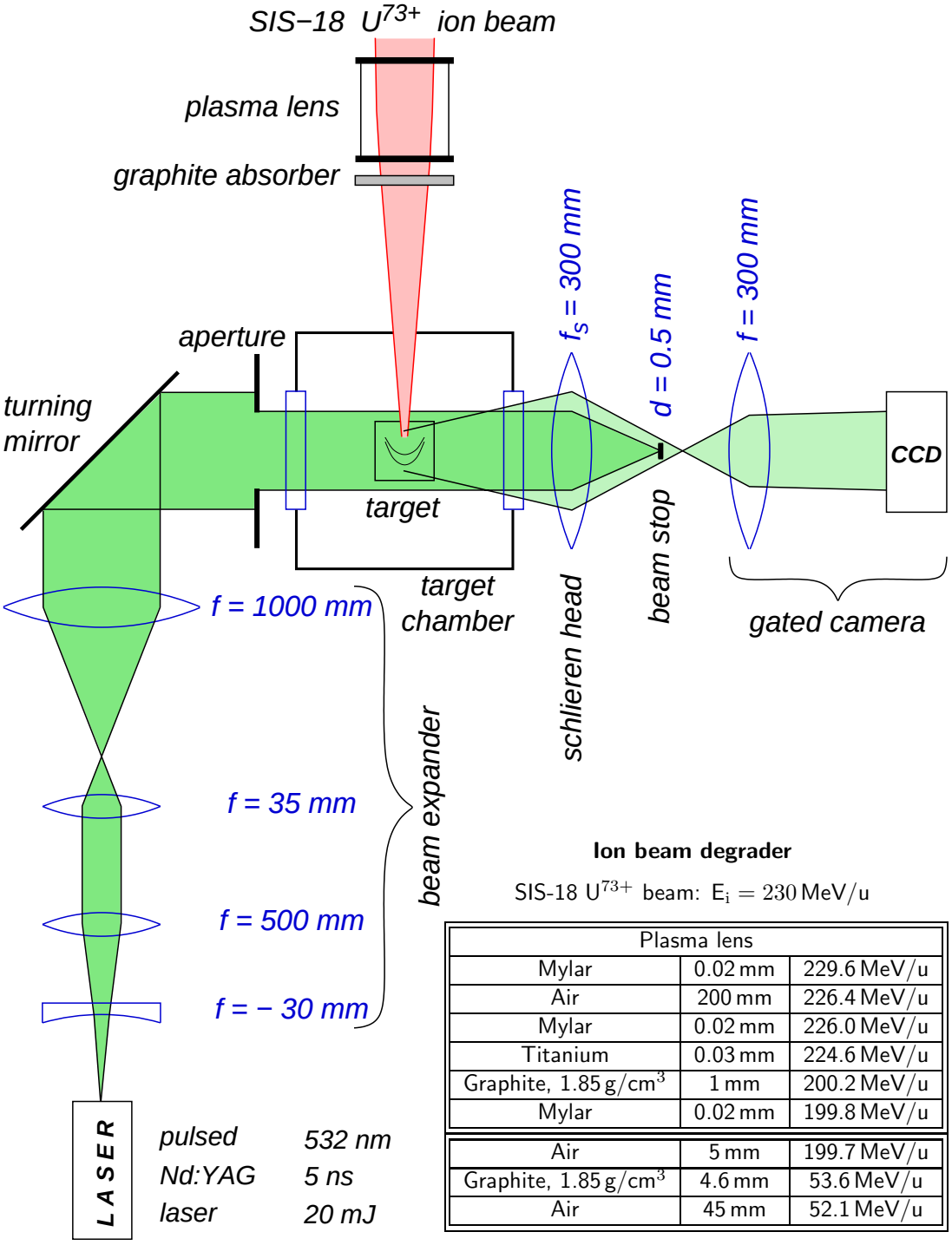

Ion beam degrader

SIS-18 U^{73+} beam: $E_i = 230\,\mathrm{MeV/u}$

Plasma lens		
Mylar	0.02 mm	229.6 MeV/u
Air	200 mm	226.4 MeV/u
Mylar	0.02 mm	226.0 MeV/u
Titanium	0.03 mm	224.6 MeV/u
Graphite, 1.85 g/cm^3	1 mm	200.2 MeV/u
Mylar	0.02 mm	199.8 MeV/u

Air	5 mm	199.7 MeV/u
Graphite, 1.85 g/cm^3	4.6 mm	53.6 MeV/u
Air	45 mm	52.1 MeV/u

Figure 3.2: Experimental set-up for the study of ion beam – matter interaction with the schlieren technique. A laser with a 5 ns long pulse ensures the time resolution in the diagnostics of ion-beam heated targets.

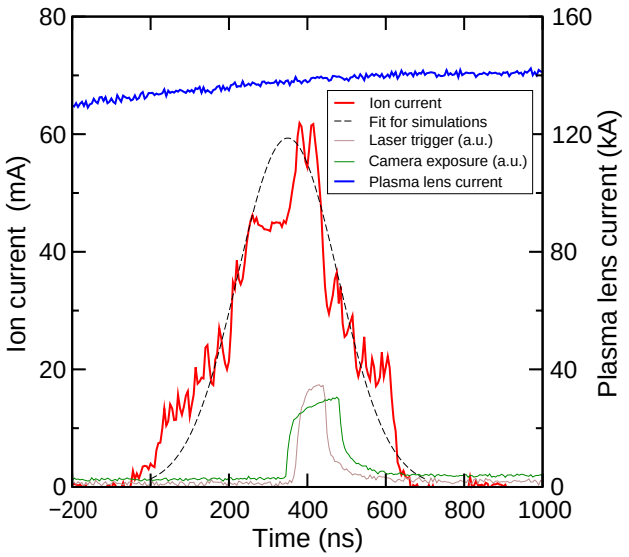

Figure 3.3: Timing for a typical schlieren image.

3.4 Results of the schlieren measurements

In this section, structure and particular details of the recorded schlieren images are discussed. The full set of the measurements will be presented in section 2.6, where the experimental results will be analyzed. A schlieren image of the fused silica (Schott Lithotec, Lithosil) sample heated by the heavy ion beam is shown in Fig. 3.4. The fused silica blocks of $10\times10\times10\,\mathrm{mm}^3$ size were polished from two sides and had a flatness $\leq \lambda/2$.

The laser rays probing the sample produce a bright image of the target without refractive index gradients caused by the ion beam. A reason for it is a wedge angle of the sample which causes deflection of the laser rays from the optical axis. Hence, the second focus occurs in the beam stop plane, different from that formed by the rays propagating outside the sample. With a beam stop of 1 mm diameter one could block both foci, but due to sensitivity reasons a beam stop with 0.5 mm diameter was used for the measurements. Comparing the alignment with the two beam stops allows to estimate the wedge angle of the fused silica samples as about 2 mrad.

The image presented in Fig. 3.4 was taken at t = 660 ns when the ion beam is still heating the sample. Besides the schlieren image of the target, scintillation along the ion beam trace in air and in the fused silica target is also recorded. As can be seen in the scaled picture of the heated region, the scintillation light along the ion beam trace in air is dislocated from the axis of symmetry of the schlieren image of the irradiated sample. Also, the light emitted in fused silica is displaced from the schlieren image of the sample.

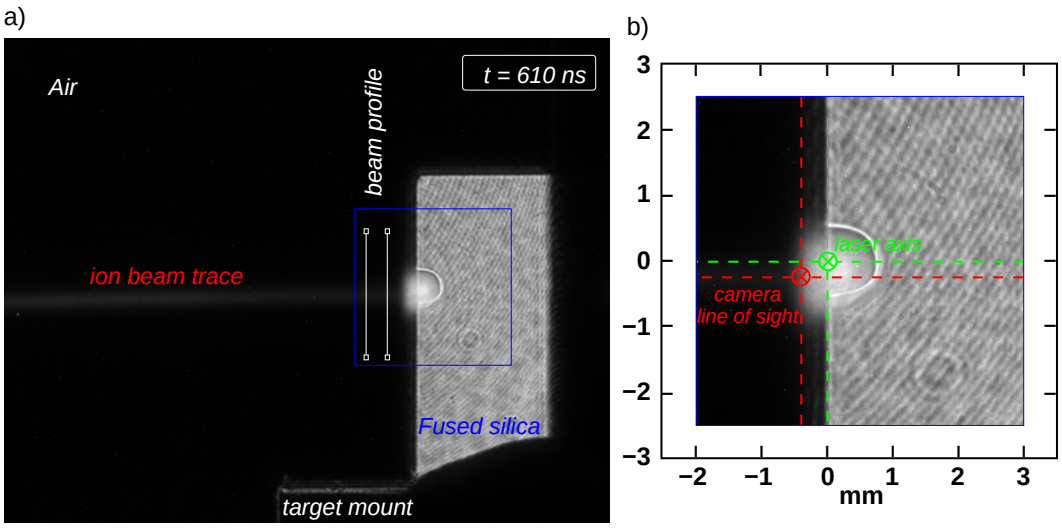

Figure 3.4: Schlieren photo of the irradiated fused silica target: a) original picture recorded by the camera, b) scaled up image of the ion beam heated area. The ion beam comes from the left side.

The displacement can be explained by the fact that pictures from two optical systems, namely schlieren and imaging of self-emission, are superposed on the camera image plane. For the schlieren set-up the optical axis and therefore the position of the image is defined by the laser axis, while for imaging of the emitted scintillation light the position of the image is defined by the line of sight of the camera. An angle between laser axis and camera line of sight leads to a shift between the two images. A misalignment of less than 1 mrad at the target position causes the observed displacement on the camera image plane.

Fig. 3.5 shows a radial profile of the ion beam trace in air at the marked position in Fig. 3.4. The exposure time of the camera was 140 ns. A Gaussian fit of this profile has a FWHM of 0.65 mm. It is a special property of the Gauss function that the projection of a two-dimensional Gauss function is a Gauss function again and FWHM for the two-dimensional and the projected functions are the same. Therefore, it is not necessary to perform an Abel transformation of the image data. Since the sound speed in gases is much less than that in condensed media, hydrodynamic motion in ion beam heated air can be neglected for at least some hundreds of ns.[1]

A schlieren photo of an ion beam irradiated water target taken at t = 1200 ns is presented in Fig. 3.6. For the experiment, cuvettes of optical quality with a wall thickness of 1 mm were filled with water. Care was taken that the water did not include bubbles, that would distort the schlieren pictures. The open side of the cuvette was sealed with 60 μm polyethylene

[1] At normal conditions air has a sound speed of 340 m/s.

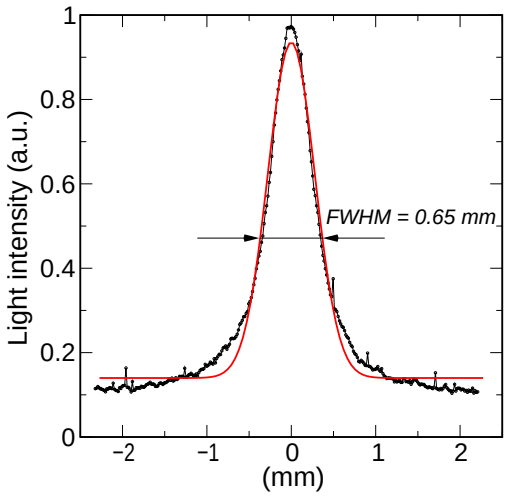

Figure 3.5: Radial profile of the ion beam trace in air due to self-emission taken with an exposure time of 140 ns. The location is marked in Fig. 3.4. A Gaussian fit has FWHM of 0.65 mm.

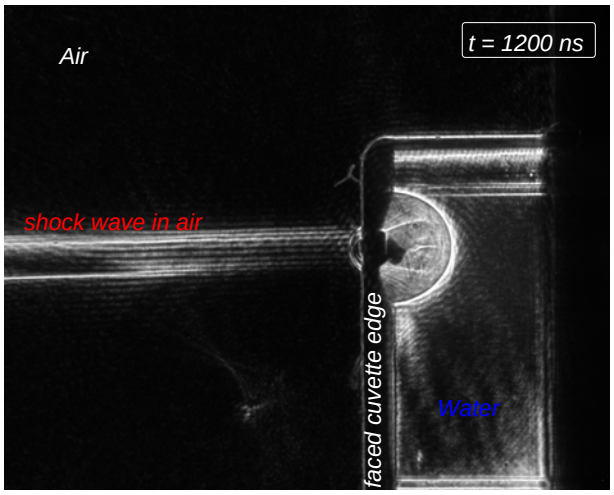

Figure 3.6: The image of the water target heated with the ion beam. The irradiated surface was sealed with a polyethylene foil.

foil and used as ion beam irradiated surface. The faced edge of the cuvette blocks the line of sight on the first 0.8 mm of the water target. Nevertheless, in some pictures, bright schlieren structures are visible in this region. This underlines that the intuitive interpretation of schlieren images as a projection of the refractive index gradients is not valid and ray-tracing modeling is required to analyze the images.

3.5 Numerical modeling of schlieren images

3.5.1 Density and temperature dependence of the refractive index

To compute schlieren images from the results of hydrodynamic simulations, the refractive index n as a function of density and temperature at the wavelength of the diagnostic light has to be known. The relation between molecular properties and the macroscopically defined parameter, n is described by the Lorentz-Lorenz equation [Jac75]

$$\gamma_{\mathrm{mol}} = \frac{3}{4\pi N}\left(\frac{n^2-1}{n^2+2}\right) \tag{3.7}$$

where γ_{mol} is the molecular polarizability, which is the ratio of the average molecular dipole moment to the applied field; N the is number of molecules per unit volume. The relation holds best for dilute substances such as gases. For liquids and solids, (3.7) is only approximately valid, especially if the dielectric constant is large.

The polarization of a collection of atoms or molecules arises in two ways:

- the applied field distorts the charge distributions and so produces an induced dipole moment at each molecule;
- the applied field tends to line up the initially randomly oriented permanent dipole moments of the molecules.

The induced (electronic) polarizability is defined by displacement of harmonically bound electrons under the action of an electric field. If there are Z electrons per molecule, f_j having a restoring force constant ($\sum_j f_j = Z$), then the molecular polarizability due to electrons is

$$\gamma_{\mathrm{el}} = \frac{e^2}{m}\sum_j \frac{f_j}{\omega_j^2}\,. \tag{3.8}$$

The second type of polarizability is that caused by the partial orientation of randomly oriented permanent dipole moments. The water molecules possess a permanent dipole moment, but it does not contribute to the polarization when the applied field is in the optical range. The orientation polarization appears only if the change of the outer field is so slow that the inertia of the molecules allows an equilibration before the field changes its direction. Therefore the orientation polarization disappears for higher frequencies, that corresponds to a wavelength of several centimeters.

The refractive index of water has been measured with care by many experiments for well over a century. Based on a comprehensive collection of

data, the following representation of the Lorentz-Lorenz function is given in [Sch90]:

$$\frac{n^2-1}{n^2+2}\frac{1}{\rho^*} = a_0 + a_1\rho^* + a_2 T^* + a_3\lambda^{*2}T^* + \frac{a_4}{\lambda^{*2}} + \frac{a_5}{\lambda^{*2}-\lambda^{*2}_{\mathrm{UV}}} + \frac{a_6}{\lambda^{*2}-\lambda^{*2}_{\mathrm{IR}}} + a_7\rho^{*2}\,, \tag{3.9}$$

where

$$\begin{array}{ll} \rho^* = \rho/\rho_0 & \rho_0 = 1\,\mathrm{g/cm^3} \\ \lambda = \lambda/\lambda_0 & \lambda_0 = 0.589\,\mu\mathrm{m} \\ T^* = T/T_0 & T_0 = 273.15\,K \end{array}$$

ρ is the density, λ is the wavelength and T is the absolute temperature. The optimized values of the coefficients a_0 to a_7, and of the effective infrared and ultraviolet resonances, λ^*_{IR} and λ^*_{UV} are listed below:

$$\begin{array}{lll} a_0 = 0.243905091 & a_1 = 9.53518094\cdot 10^{-3} & a_2 = -3.64358110\cdot 10^{-3} \\ a_3 = 2.65666426\cdot 10^{-4} & a_4 = 1.59189325\cdot 10^{-3} & a_5 = 2.45733798\cdot 10^{-3} \\ a_6 = 0.897478251 & a_7 = -1.63066183\cdot 10^{-2} & \\ \lambda^*_{\mathrm{IR}} = 5.432937 & \lambda^*_{\mathrm{UV}} = 0.2292020 & \end{array}$$

The fit uses data which exist for the following range of the three independent variables:

$$\begin{array}{ll} \text{temperature} & 0 < T < 225^{\circ}\mathrm{C} \\ \text{density} & 0 < \rho < 1.06\,\mathrm{g/cm^3} \\ \text{wavelength} & 0.2 < \lambda < 2.5\,\mu\mathrm{m} \end{array} \tag{3.10}$$

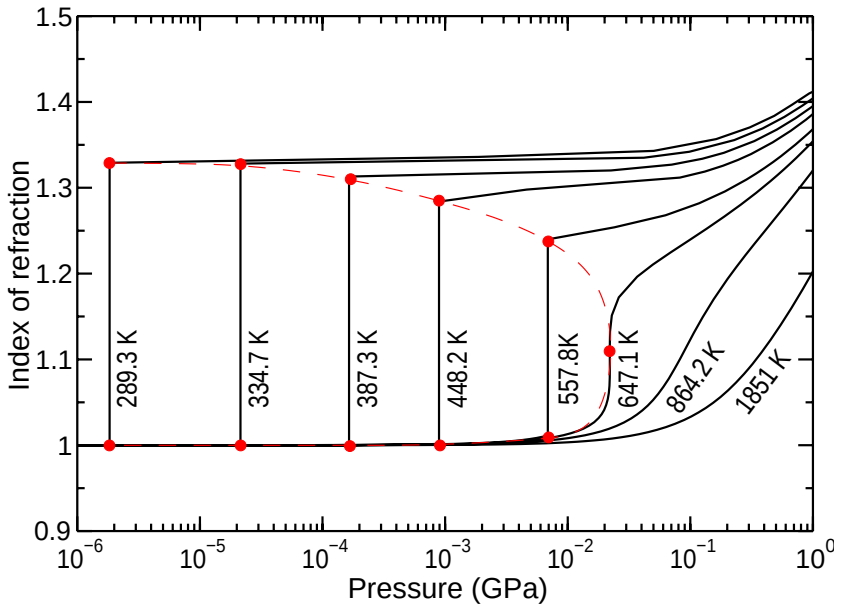

Figure 3.7: Refractive index of water as a function of pressure and temperature. Red points indicate the evaporation curve.

It is expected, but cannot be substantiated by comparison with data, that the formulation (3.9) will give estimates of the refractive index at temperatures much higher than given in (3.10), and that it will extrapolate correctly even into the supercritical regime.

Fig. 3.7 shows the refractive index of water as calculated from (3.9) for $\lambda = 532\,\mathrm{nm}$, that was the wavelength of the schlieren laser at the experiment, as function of pressure and temperature. The SESAME equation of state for water # 7152 was used to convert density to pressure. The SESAME data were modified introducing a Maxwell construction in the subcritical region.

The density of the fused silica, as for any given substance, is proportional to $(n^2-1)/(n^2+2)$ according to the Lorentz-Lorenz equation. The variation of the refractive index with temperature is [Mal65]

$$\frac{dn}{dT} \approx 1.1 \cdot 10^{-5}\,\mathrm{K}^{-1}\,. \tag{3.11}$$

It is evident that dn/dT must result from a change in the internal structure of the material with temperature. The dilution of dispersive material by thermal expansion would tend to produce a negative dn/dT, opposite to what is observed.

3.5.2 Ray-tracing simulations

When density, temperature and wavelength dependence of the refractive index, $n(\rho, T, \lambda)$ are known, one can obtain computed schlieren images by modeling the propagation of laser rays in the sample. Interaction of heavy ion beams with matter is calculated with the help of a two-dimensional hydrodynamic code in cylindrical geometry using an adaptive grid. To perform ray-tracing calculations it is convenient to map the results of hydrodynamic simulations into a regular 3D Cartesian grid.

The IDL (Interactive Data Language) computing environment was used to regularize the 3D distribution of the refractive index, $n_i(x_i, y_i, z_i)$ over a regular grid, applying a method described in [Ren88], which has been referred as Modified Shepard's Method. The fitted function determined by this method has the advantages of being equal to the values of n_i at each (x_i, y_i, z_i) and being smooth (having continuous first partial derivatives).

Fig. 3.8 shows the distribution of the refractive index on the regular grid in the center of the ion beam heated target. Hydrodynamic simulations were performed with the BIG-2 code [For96] using the SESAME [SES83] equation of state tables. The calculated case corresponds to the experimental schlieren image for water at $t = 660\,\mathrm{ns}$ (see section 3.6). The ion beam is coming along the z-axis, the diagnostics laser rays probe the target along the x-axis. The cell size of the regular grid was taken small enough to describe details of the hydrodynamic flowfield. The dashed line shows the position of the cross-section plotted in Fig. 3.9.

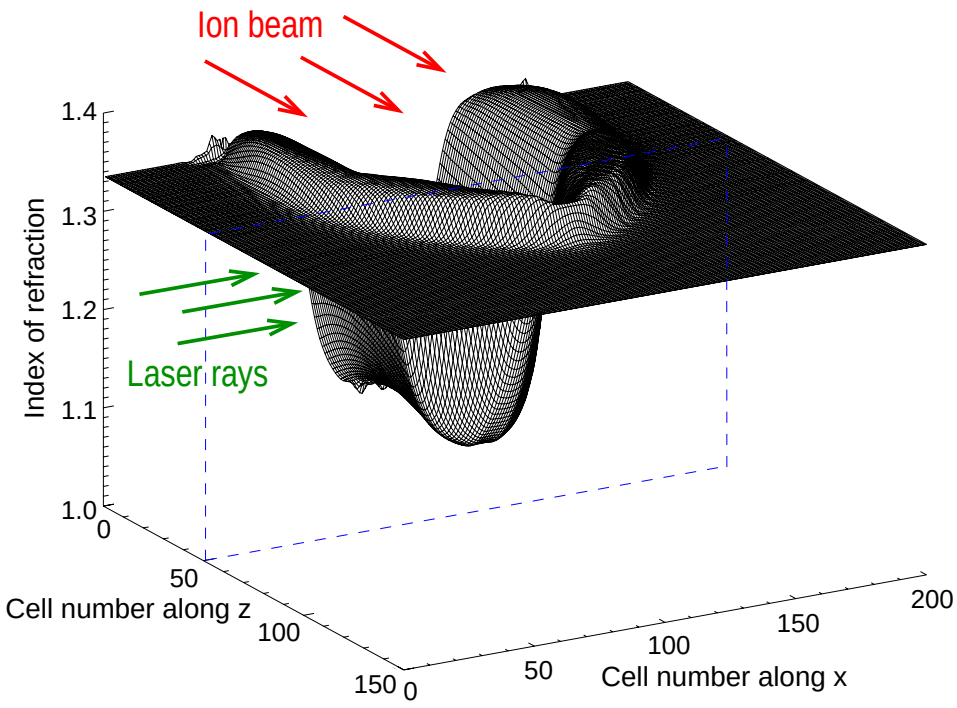

Figure 3.8: Distribution of the refractive index in the center of water target at $t = 660\,\text{ns}$. Beam parameters: 2×10^9 U ions of 52 MeV/u energy, pulse duration 300 ns (FWHM), Gaussian radial profile with FWHM of 650 μm.

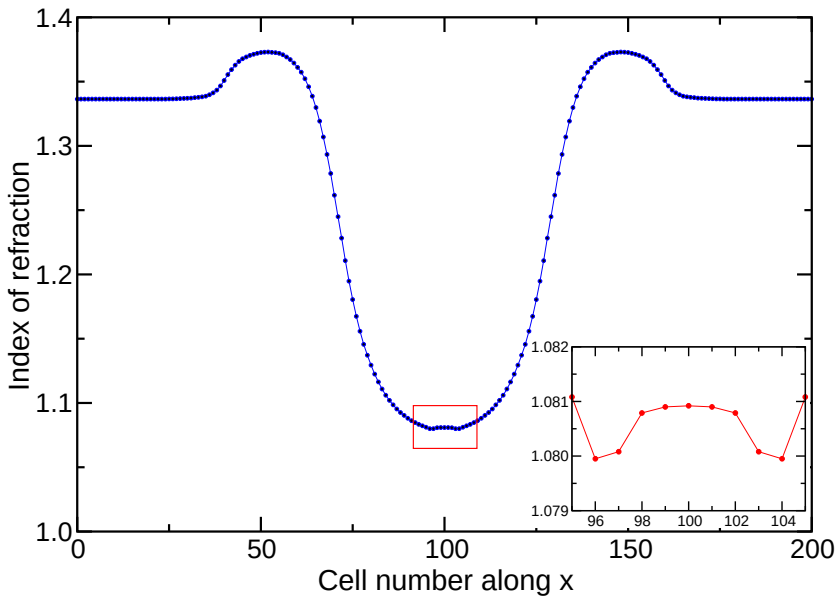

Figure 3.9: Plot of the refractive index in the water target in the plane shown in Fig. 3.8.

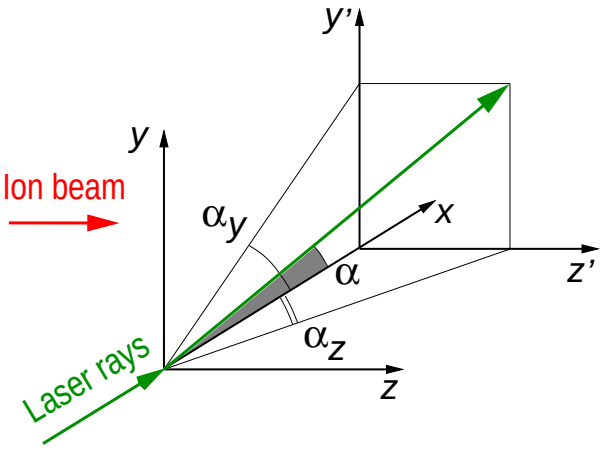

Figure 3.10: Depiction of the deflection angle.

As it can be seen from Fig. 3.9, an unphysical increase of the refractive index occurs in the vicinity of the symmetry axis. The region of such a growth in the refractive index corresponds to the central cell in hydrodynamic simulation. Note, that this behavior of the refractive index near the target axis will distort the calculated schlieren image.

In the approximation of geometrical optics, the deflection angle of a ray in a heterogeneous medium is defined by equation (3.5), where integration is performed along the ray path. The deflection angle can be presented as a sum of two components, α_y along the y-axis and α_z along the z-axis (see Fig. 3.10). If the deflection angle is small, the integration along the real ray path can be replaced by integration along the incidence direction of the ray, i.e. the x-axis. Hence, the deflection angles α_y and α_z can be calculated as

$$\alpha_y = \int \frac{1}{n}\frac{\partial n}{\partial y}\,dx\,, \qquad \alpha_z = \int \frac{1}{n}\frac{\partial n}{\partial z}\,dx\,. \tag{3.12}$$

Taking into account the beam stop of the schlieren set up, deflection angles $\alpha = \sqrt{\alpha_y^2 + \alpha_z^2}$ smaller than the $\alpha_{\min}$ defined in (3.6) do not contribute to the schlieren image.

3.6 Analysis of the experimental results

In this section the results of the schlieren measurements are analyzed. To interpret the obtained experimental data, computed schlieren images were constructed out of hydrodynamic simulations by ray-tracing modeling. The targets were made out of two different materials, namely water and fused silica. First, the ion beam heating of water targets will be considered.

Water targets at different times after the heavy ion beam heating are shown in Fig. 3.11. The ion beam consists of 2×10^9 U ions with an energy

of 52 MeV/u. The time evolution of the ion current was fitted by a Gaussian profile with FWHM of 300 ns as shown in Fig. 3.3. The beam was focused down to a diameter of about 650 μm (FWHM of a Gaussian fit). The time resolution of the schlieren system was provided by the probing laser with a pulse duration of 5 ns. The behavior of the targets is shown at $t = 660$ ns which is near to the ion pulse end, and later at $t = 1200$ and 1800 ns, when a shock wave propagates in the target.

Figure 3.11a shows the experimental schlieren images of the water targets. Details of the recorded schlieren photos were discussed in section 3.4. To analyze the experimental results, schlieren pictures were constructed from the results of a hydro simulation using the above ion beam parameters. The interaction of the ion beam with the water targets was simulated with the hydrodynamic code BIG-2 [For96] using the SESAME equation of state [SES83] # 7152 which was modified introducing a Maxwell construction. For $t = 660$ and 1200 ns the 60 μm polyethylene foil that was sealing the water target was included in the simulations, while for $t = 1800$ ns the foil had to be omitted due to numerical problems. Equation (3.9) was used to calculate the distribution of the refractive index from the density and temperature fields of the hydrodynamic simulations. The schlieren images were computed by modeling the laser ray propagation in the 3D sample with a given refractive index field. Fig. 3.11b shows the calculated schlieren images corresponding to the experimental data. Red lines mark the faced edge of the cuvette, where the line of sight was blocked. To interpret the schlieren pictures and the target behavior, the calculated density and phase distributions are shown in Fig. 3.11c and d.

Both experimental and computed schlieren pictures have a spherical structure with a radius that is increasing with time. The rate of expansion is the same for the measured and simulated images. Hence, an overall agreement can be stated, but several details are different in the experimental and modeled pictures. First, on the computed image for $t = 660$ ns, distortions in the vicinity of the target axis are clearly seen. Second, the dark region in the center of the simulated structures is considerably larger than the corresponding structure in the experimental images. Third, the computed pictures show a dark region just behind the outer edge of the spherical schlieren structure, that is missing in the experimental images.

The reason for the distortions near the axis, which are mainly seen in the first picture are caused by numerical problems in the central cell of the hydrodynamic calculations, as was noted in section 3.5.2. The artificial gradient at the axis leads to a deflection of light and therefore the spherical structure is not visible at the axis. Also, the gradients are so high that deflected light forms a vertical line near the front of the schlieren structure.

The dark region in the center of the schlieren structure can be interpreted as a phase boundary between liquid and gas. As it is seen in Fig. 3.11c and

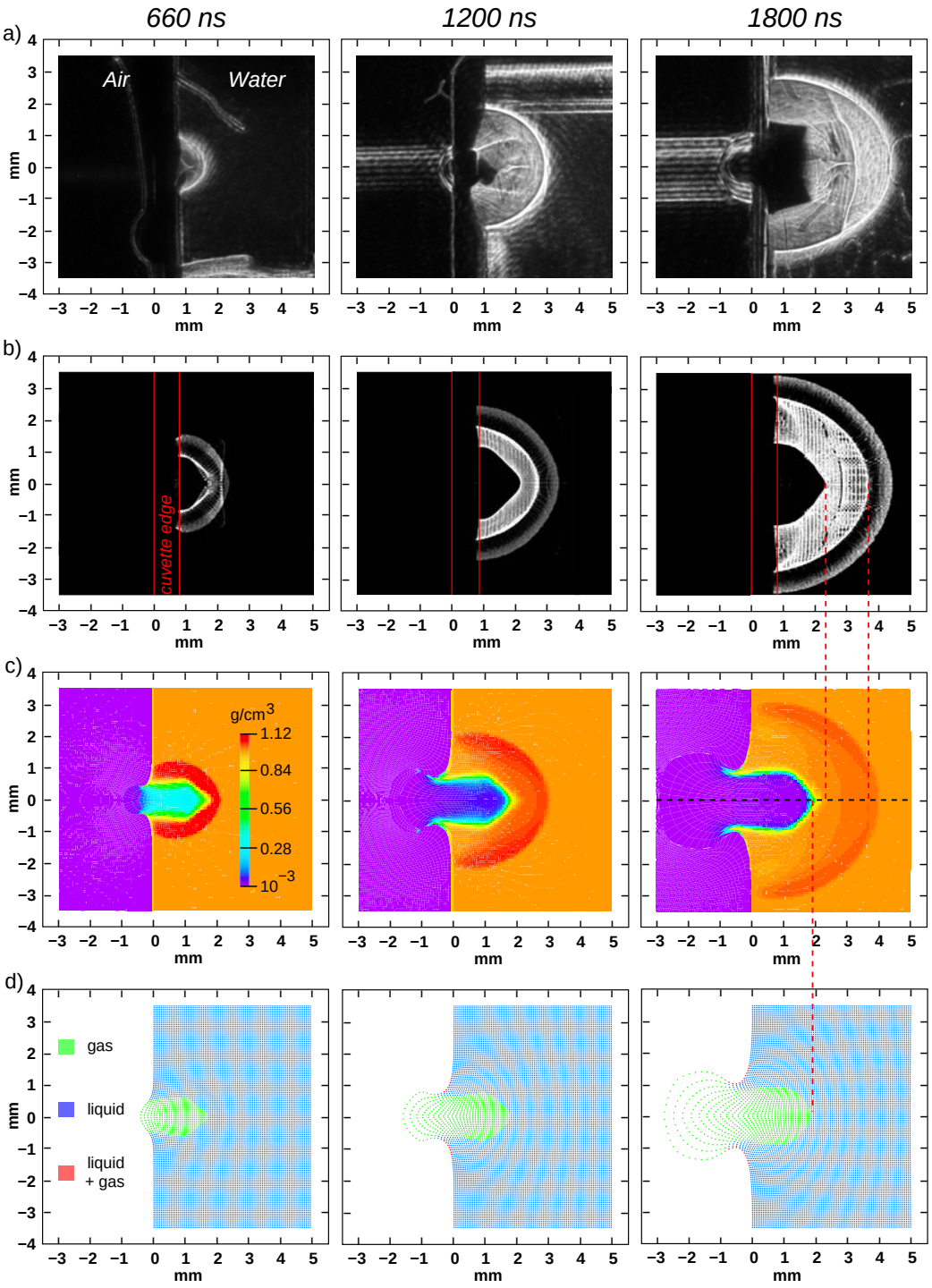

Figure 3.11: Water target at different times: a) schlieren images; b) computed schlieren images; c) density distributions calculated with hydro code; d) regions of gas and liquid phases.

d, the phase boundary corresponds to the largest density step. Comparison of b and c shows that the schlieren structure corresponding to this gradient is shifted towards the direction of higher density in the simulated schlieren picture. The same shift of structures in the schlieren image is responsible for the dark region just behind the outer edge of the spherical schlieren structure.

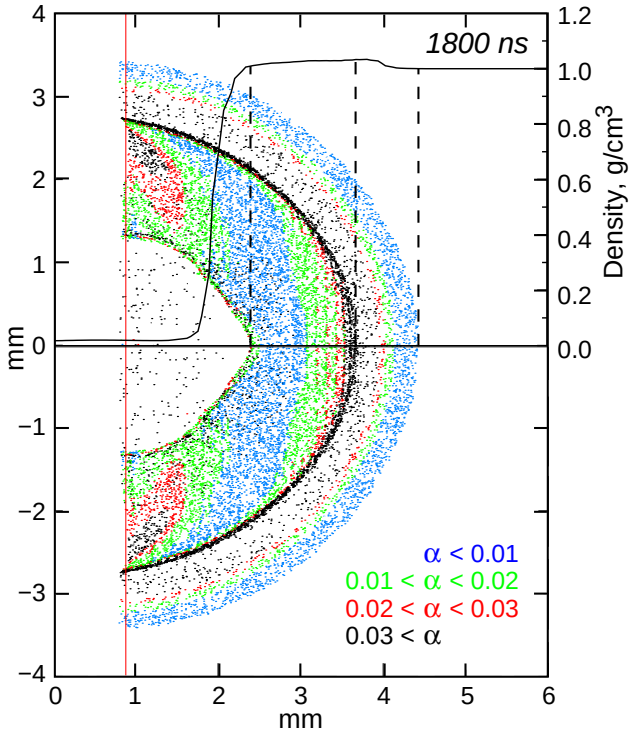

Figure 3.12: Distribution of deflection angles at t=1800 ns and target density along the axis.

This effect is explained in Fig. 3.12. The computed schlieren image for $t = 1800$ ns includes a color representation of the deflection angles. The density profile along the target axis is also shown. The structures on the schlieren image are shifted to the region of higher density, i.e. higher refraction index. The illustration of this phenomena was presented in section 3.2. Note that the shift of the schlieren structures increases with the length of the light path in the schlieren object and with the strength of the gradient. This means the shift is larger for big schlieren objects and for strong gradients. The gradient along the phase boundary shifts the corresponding schlieren structure to larger radii, and therefore increases the dark region compared to the calculated phase boundary from the hydro simulations. The same effect leads to a shift near the outer edge of the schlieren structure. Here the shift is again to the high density region and therefore towards smaller radii. Since the gradients at the shock front are increasing the shift is increasing, leading

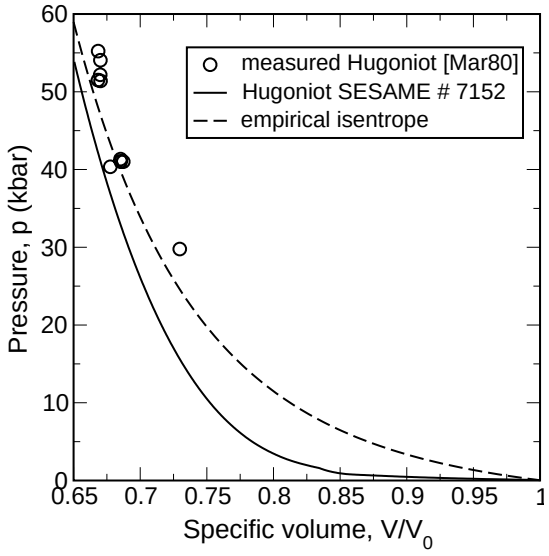

Figure 3.13: Principle Hugoniot and isentrope for water.

to a zone of reduced light intensity (the dark region behind the outer edge of the schlieren structure). The deflected light concentrates where the gradients are becoming smaller, and forms the intense black ring at a radius of about 3 mm in Fig. 3.12.

Comparing the computed and experimental schlieren images shows that the phase boundary in the experimental imaged is located at smaller radii. Also the dark zone near the front of the schlieren structure is absent, which indicates smaller density gradients than in the simulation. Both effects can be connected to the equation of state used in the numerical simulations. To validate the used EOS, the principle Hugoniot calculated from the EOS was compared with measured data [Mar80] and with an empirical isentrope (see Fig. 3.13).

When the shock compression of matter is weak, the entropy change across the shock can be neglected, and an adiabatic equation of state can be used. To describe the isentropic flow region, the following empirical equation of state for a condensed material is frequently used

$$p = A(S)\left[\left(\frac{V_0}{V}\right)^n - 1\right], \tag{3.13}$$

where n is constant and A slightly depends on entropy. The coefficients A and n are related by an equation which includes the sound speed at standard conditions

$$c_0^2 = -V_0^2\left(\frac{\partial p}{\partial V}\right)_S = V_0 A n\,. \tag{3.14}$$

For water, $n \approx 7-8$ and $A = 3\,\mathrm{kbar}$ [Zel67]. The energy equation (2.4) with $p_0 = 0$ can then be used to estimate the increase of internal energy due to

irreversibility of the shock compression. The difference

$$\Delta\epsilon = \frac{1}{2}p(V_0 - V) - \int_V^{V_0} (p\,dV)_{S=const}\,, \tag{3.15}$$

is by definition equal to the increase in internal energy caused by the entropy increase across the shock wave. The smaller this value is in comparison to the total energy increase across the shock wave $\epsilon - \epsilon_0$, the better is the "adiabatic" approximation of the shock compression.

Calculation of the ratio $\Delta\epsilon/(\epsilon - \epsilon_0)$ for n=7 and $V_0/V = 1.1$ gives 14%, independent from A. For water, a compression of 1.1 corresponds to a pressure of 2.9 kbar. Thus, for pressures less than 3 kbar a shock wave in water can be regarded as an acoustic wave with an error in energy of 14%, the error in pressure is even less.

It is known from the shock compression theory that the Hugoniot should be located above the isentrope. This condition is not satisfied for the SESAME equation of state used in the calculation. As is seen from the plot, the Hugoniot extracted from the SESAME data corresponds to a higher compressibility of matter than the empirical isentrope. This can explain, that the phase boundary in the experimental schlieren images has a smaller radius than in the calculations, and that the gradient at the shock front is weaker. Therefore the discrepancies of the simulated schlieren images to the experiments can mainly be attributed to the imperfection of the used SESAME equation of state.

Fused silica was chosen as the second target material for the schlieren measurements. The range of 52 MeV/u uranium ions in fused silica is $R = 0.68$ mm according to the SRIM [Zie01] code. Fig. 3.14 shows schlieren pictures of the ion beam heated fused silica targets at $t = 610$, 830, 1450 ns and 10 ms. The schlieren structure in the first three images has a size which can be related to the ion beam deposition zone; the length corresponds to the range of the beam ions in fused silica. At the last picture, at $t = 10$ ms, the schlieren structure is larger by about 0.2 mm. There is no shock wave visible in the heated fused silica target.

To make a simple estimate of the parameter regime achieved in the irradiated sample, isochoric, i.e instantaneous heating of the target can be assumed. An ion beam with the above parameters has an energy of about 4 J. Let us assume, that this beam energy is uniformly deposited in a cylinder with a length equal to the ion range R and a radius of 0.7 mm. The total internal energy after irradiation will be, according to SESAME, $\epsilon = 1.9$ kJ/g. The maximum pressure is $p_{\max} = \Gamma\rho_0\epsilon = 80$ kbar, where $\Gamma = 1.9$ is the Grüneisen parameter for fused silica; $\rho_0 = 2.204\,\mathrm{g/cm^3}$ is the initial density. The corresponding temperature is $T_{\max} = 1650$ K.

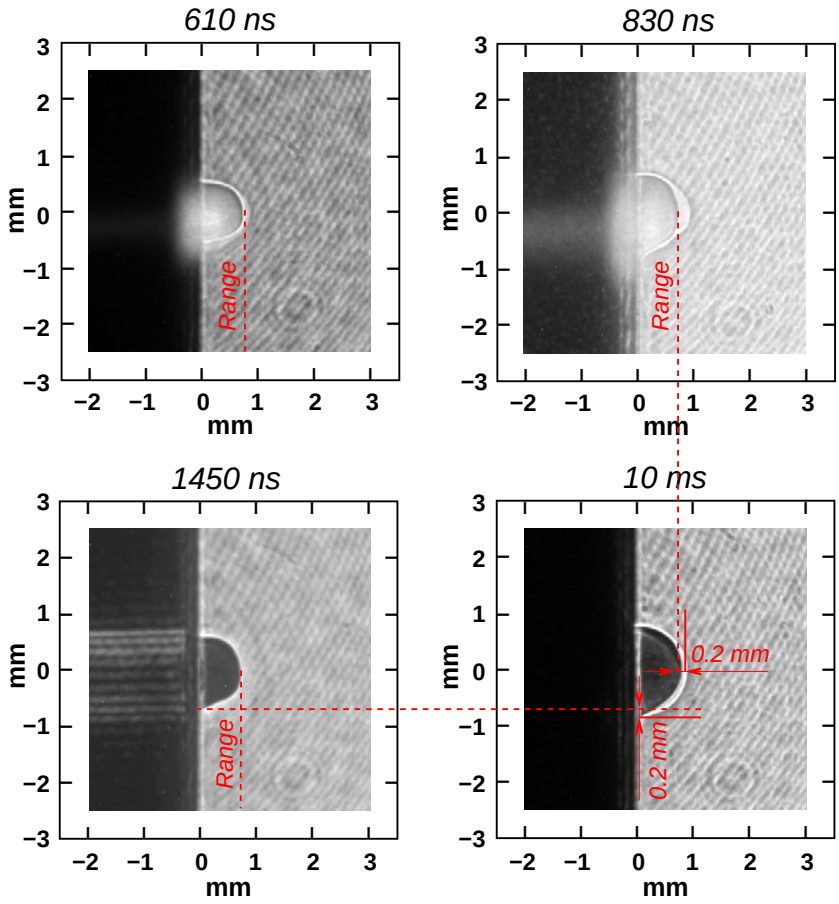

Figure 3.14: Schlieren images of fused silica target at different times.

A compression wave in a solid body is treated as a strong compression wave (shock wave) and examined in hydrodynamic approximation, if the pressure generated in this wave exceeds the Hugoniot elastic limit (HEL), σ_g, for a given material

$$\sigma_g = \frac{2\sigma_T}{3\,(1 - c_0^2/c_l^2)}\,. \tag{3.16}$$

Here σ_T is the dynamic yield point, c_0 is bulk, and c_l is longitudinal sound speed. For fused silica $c_0 = 3.77\,\mathrm{km/s}$, $c_l = 5.96\,\mathrm{km/s}$, and $\sigma_T = 72\,\mathrm{kbar}$. This leads to a HEL of $\sigma_g = 80\,\mathrm{kbar}$. The pressure in a shock wave in front of the heated zone can be estimated as

$$p_{\mathrm{shock}} = \frac{p_{\max}}{2} = \frac{\Gamma\rho_0\epsilon}{2} = 40\,\mathrm{kbar}\,. \tag{3.17}$$

The pressure in the shock wave p_{shock} is smaller than the HEL, therefore only weak acoustic compression wave is generated in the sample.

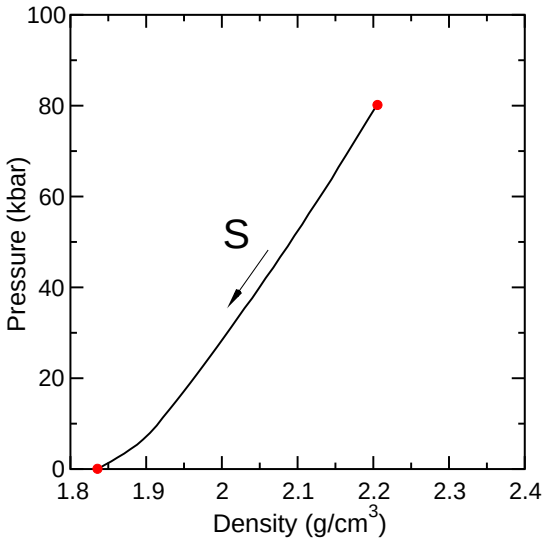

Figure 3.15: Expansion isentrope calculated from SESAME # 7380. Initial and final points are marked in red.

The energy release of the ion beam in the sample does not set material into motion. While the surface of the target is free, and the heated region is situated in the vicinity of the target surface, an isentropic expansion of the heated zone to the ambient pressure can be assumed. Fig. 3.15 shows an expansion isentrope extracted from the SESAME equation of state for fused silica. The initial point corresponds to the pressure $p_{\max}$ and the normal density ρ_0. At atmospheric pressure the density will be equal to $\rho_1 = 1.84\,\mathrm{g/cm^3}$, the temperature $T_1 = 1140\,\mathrm{K}$. According to the Lorentz-Lorenz equation (3.7), the change of the refractive index related to the dilution of the target material is $\Delta n_\rho = -0.09$. The temperature dependence of the refractive index will produce $\Delta n_T = 0.01$ according to (3.11). Therefore, the schlieren pictures show the density gradients. The broadening of the gradient in beam direction in the picture for $t = 830\,\mathrm{ns}$ can be explained due to compression of the material in front of the heated region.

If the hydrodynamic energy transfer is unimportant, heat is transported by thermal conduction. The transport of thermal disturbances through a medium by ordinary heat conduction is comparatively slow. Weak pressure disturbances propagate with the speed of sound, and the pressure equalizes more rapidly than the temperature. The acoustic relaxation time of the heated zone can be defined as [Efr94]

$$t_\mathrm{r} = \frac{R}{c_\mathrm{l}} \approx 100\,\mathrm{ns}\,, \tag{3.18}$$

if the change of the sound speed due to heat is neglected. During this time the rarefaction wave from the surface propagates across the heated region.

Using equation (2.41) for the rate of the spherical thermal wave propagation, the coefficient of thermal diffusivity can be estimated from the experimental schlieren images as:

$$\chi \sim \frac{\Delta r^2}{4\Delta t}\,. \tag{3.19}$$

For $\Delta r = 0.2\,\mathrm{mm}$ and $\Delta t = 10\,\mathrm{ms}$ one gets $\chi \approx 0.01\,\mathrm{cm}^2/\mathrm{s}$. This corresponds to a temperature of about 1100 K. Equation (2.41) describes the diffusion of a Gaussian temperature profile $\exp(-r^2/\sigma^2)$ at a radius equal to σ.

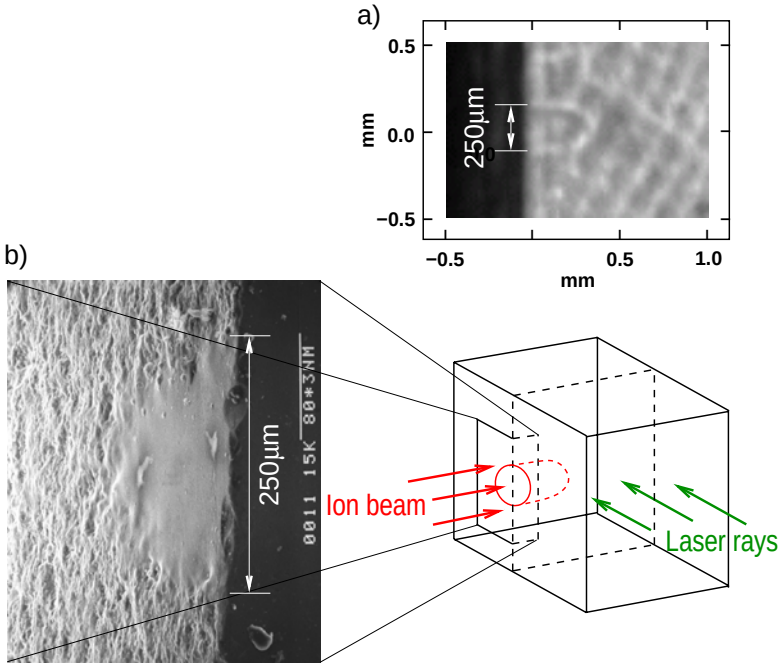

Figure 3.16: a) Schlieren photo of fused silica target after irradiation. b) Electron microscope (REM, tilt angle 22°) image of target cut through the irradiated area.

Figure 3.16a shows a schlieren image of the target 15 min after ion beam irradiation. On this picture a gradient inside the heated zone is visible. To interpret the origin of this structure, the irradiated sample was cut along a plane through the heated area. An electron microscope (REM) image of the cut target is presented in Fig. 3.16b. Although the reason for the gradients could not be found in the REM image along the cut plane, the smoothing of the irradiated target surface with a diameter equal to the structure in the schlieren image was found. Here, the originally unpolished surface had obviously been liquid, but definitely below the evaporation temperature since no crater was formed. An explanation for the schlieren image after irradiation

can be a different glass structure due to the fast cooling of the liquid zone. Evaporation of fused silica occurs at a temperature T_e =2400 K, the material has a softening point of T_s = 1880 K.

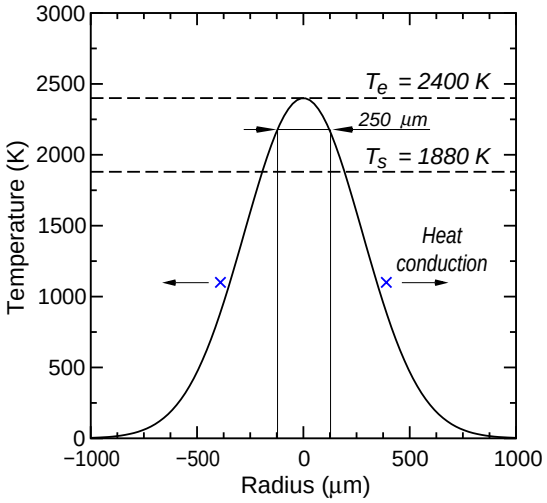

Figure 3.17: Estimation of the temperature profile in the target. The blue points are the σ-values at the distribution defined from the heat wave propagation.

Figure 3.17 shows an estimation of the radial temperature profile in the target at the end of the beam pulse. The Gaussian profile has a FWHM of 0.65 mm like the ion beam. The maximum temperature is taken to be equal to T_e, since it is clear that the target material was not evaporated. According to this assumption, the surface smoothing with a diameter of 250 μm occurred at a temperature above the softening temperature T_s, that can be expected. The temperature value defined from the heat wave propagation rate corresponds well to this assumed temperature distribution.

Chapter 4

Advanced targets for equations of state measurements with heavy ion beams

Most experimental data on the thermodynamic properties of matter at high energy densities are measured in shock wave experiments [Alt65]. In those experiments, a shock front passes through a sample with known initial density and pressure, and two physical quantities are measured: the shock velocity and the post-shock matter velocity. Then the laws of conservation of mass, momentum, and energy allow to calculate the pressure, p, and density, ρ, in the compressed state, as well as the specific energy, ϵ. In this way one point $p = p(\rho, \epsilon)$ is obtained for so called "caloric" equation of state. This kind of equation of state measurements requires a planar shock wave geometry, which is usually not provided in the case of an ion beam launched shock. Therefore an advanced target design to create a planar shock wave with the currently available heavy ion beam is proposed in section 4.1.

Intense beams of energetic heavy ions have the beneficial property to deposit their energy with good uniformity over an extended volume, as long as the Bragg peak remains outside the heated region. The stopping power of most materials is fairly well known. Hence, with a given beam current density profile, the total deposited specific energy is known with a good accuracy. When the density of the heated sample, ρ_0, remains unchanged, the thermodynamic state of matter after irradiation is completely defined by the two quantities ϵ and ρ_0. In this case it is sufficient to measure one physical quantity to obtain a meaningful point for the caloric EOS. The dynamic confinement [Koz03] proposed in section 4.2 is aimed at suppressing the hydrodynamic motion during heating by ion beam and maintaining a constant density sample, which allows x-ray scattering diagnostics.

4.1 Generation of a planar shock wave

Direct determination of the equations of state of shock compressed matter requires a planar shock wave geometry. The evaluation of measurements in other geometries requires hydrodynamic simulations, which depend on the EOS data. In this section, possibilities to create a planar shock wave in matter heated by intense heavy ion beams are examined. The proposed target configurations allow to perform EOS measurements of shock compressed matter with the present ion beam parameters.

Heavy ion beams deposit their energy deep in the target volume. The stopping power of a single ion is known with good accuracy and defined by the Bragg curve. Basic principles of heavy ion deceleration in matter were discussed in section 2.2. However, the energy deposition of an ion beam in matter depends strongly on the duration and intensity of the beam pulse due to hydrodynamic motion of the target material during the heating time. The SIS-18 synchrotron at GSI is currently able to provide up to 5×10^9 uranium ions accelerated to 200 MeV/u delivered in a single pulse of 500 ns length. A quadrupole focusing system allows to focus the beam down to 0.5 mm (FWHM of a Gaussian profile).

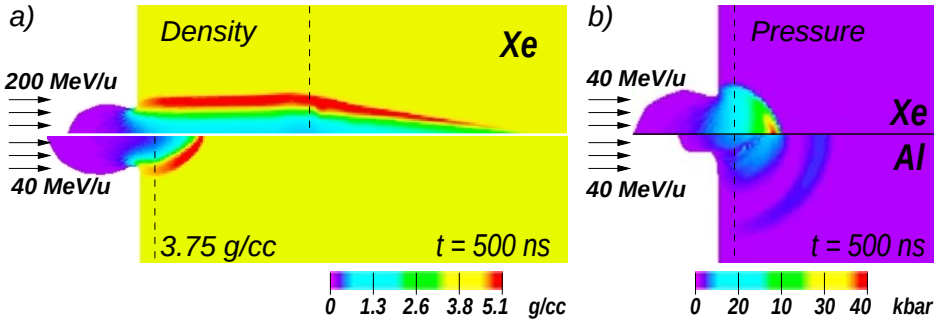

Figure 4.1: a) Density in solid xenon irradiated with 200 MeV/u U ions (top) and 40 MeV/u U ions (bottom), b) pressure in xenon (top) and in aluminum (bottom). The ion beam pulse consists of 5×10^9 particles.

Fig. 4.1a (top) shows the density distribution in a solid xenon target irradiated with such a beam. Simulations were carried out with the 2D hydrodynamic code BIG-2 [For96] supplemented by the SESAME equation of state data [SES83]. The dashed line shows the initial position of the Bragg peak. The decrease in the target density near the axis due to the radial shock wave allows the ions to penetrate deeper into the target. Due to the Gaussian spatial profile of the beam current, the density starts to decrease in the vicinity of the axis from the very beginning of the ion pulse. The increase of the ion range during the heating time was also discussed in [Arn87]. The ion beam was assumed to be uniform within sharp spatial boundaries.

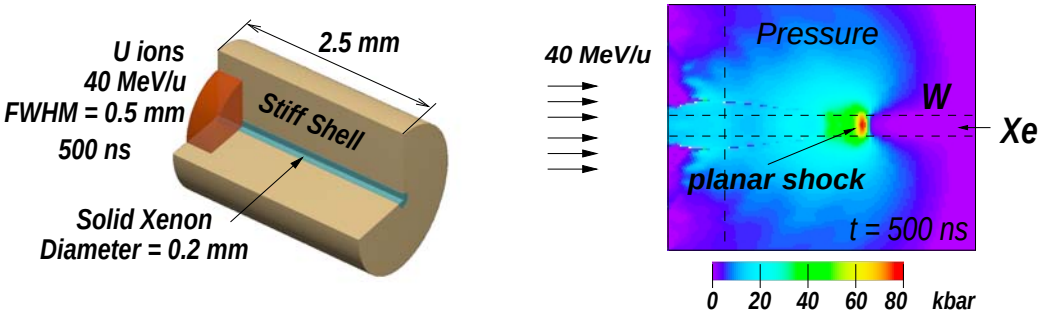

Figure 4.2: Pressure in a low diameter xenon tube surrounded by a tungsten shell after irradiation with 5×10^9 U ions of 40 MeV/u energy.

The effect of the range lengthening can be avoided with a low energy beam. The density distribution in xenon irradiated with a 40 MeV/u beam is shown in Fig. 4.1a (bottom). According to the simulations, the Bragg peak location does not change and the shock wave has almost spherical shape. The shock wave induced by the ion beam becomes stronger if a target material with a low sound speed is used. In Fig. 4.1b the pressure distribution in solid xenon which has a sound speed of 1 km/s and in aluminum, with a sound speed of 5.3 km/s are compared.[1] Significantly less hydrodynamic motion is induced in the case of xenon.

To create a planar shock wave in ion beam heated matter, a low diameter tube surrounded by a stiff shell can be used. The target consists of a tungsten shell which contains frozen xenon. Fig. 4.2 shows the pressure distribution for such a target irradiated with a 40 MeV/u beam with the above parameters. The vertical dashed line shows the position of the Bragg peak in xenon. The diameter of the xenon core is 0.2 mm, which is about half of the FWHM of the Gaussian beam current density profile. During the deposition time a shock wave starts to propagate in the xenon in forward direction. The stiff tube surrounding the xenon core forms a planar shock wave from the initially inhomogeneous target loading by the ion beam. Numerical simulations predict a pressure of 80 kbar, a density of 5.8 kg/cm^3, and a temperature of about 700 K behind the planar front.

The "hardness" of the material for a weak shock wave is characterized by the product of density and sound speed, ρc, which is called acoustic impedance. It determines the relation between pressure and velocity in an acoustic or a weak shock wave, with $p = \rho c u$. For a strong shock, a similar quantity was defined in section 2.1. Consider the passage of a weak shock wave from material A to material B. The wave traveling through material B

[1]The Hugoniot elastic limit of aluminum is approximately 6 kbar. Therefore, hydrodynamic description can be applied in this calculation.

is always a shock wave, while the wave reflected in A is either a shock wave, in case material B is "harder" than A, $\rho_B c_B > \rho_A c_A$, or a rarefaction wave, in case B is "softer" than A.

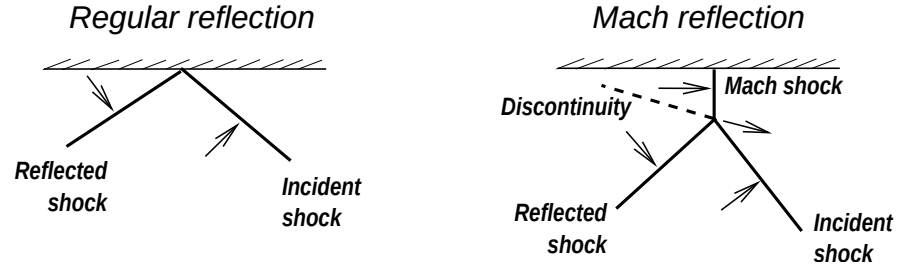

Figure 4.3: Regular and irregular, or Mach reflection of a shock front on a rigid surface.

The phenomena occurring by reflection of a shock from a rigid surface can be used to produce a planar front in ion beam heated matter. Reflection of a shock wave on a rigid wall results in a considerable increase of the pressure. The simplest type of reflection occurs when the reflected wave leaves the line of intersection itself (see Fig. 4.3). This is called regular reflection, and in a perfect gas it can be described analytically [Cou99].

Regular reflection becomes impossible if the incident shock is made sufficiently strong, or if a strong shock front impinges on a zone of rest at an angle almost perpendicular to the rigid wall. The incident shock wave breaks up at a distance from the surface, so that one has a pattern with three shock waves and a tangential discontinuity leaving the point where the incident shock wave divides. This is called Mach reflection. The Mach shock wave is produced at the point of intersection and the pressure in this wave is higher than in the incident wave. An exact analytical description of the Mach reflection cannot be constructed.

Very high shock compression pressures can be produced by irregular reflection of oblique incident shock waves. The phenomenon of irregular reflection is used in conical explosion devices to study the equation of state of materials in the megabar pressure range [Bus93],[Gra93]. Fig. 4.4 shows a novel target configuration to generate a planar shock in ion beam loaded matter and calculated pressure distributions for different times. The target consists of a tapered tube made of tungsten filled with solid xenon. The parameters of the tube were adapted numerically to the above given SIS-18 ion beam parameters currently available at GSI. Understanding of the particular details of shock propagation and reflection in such a complicated target requires an extensive numerical study.

The tube is irradiated from the wide side with a low energy beam. The entire diameter of the tube is such that the beam does not heat the tungsten

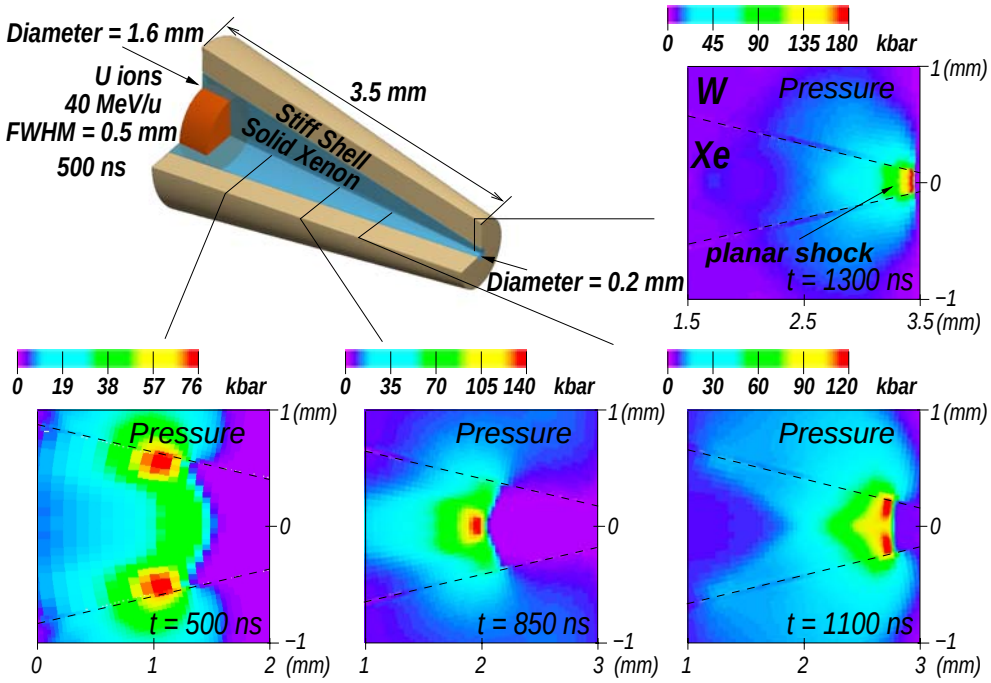

Figure 4.4: Pressure in a tapered tube, irradiated with 40 MeV/u U ions, at different times. The ion beam consists of 5×10^9 U ions.

shell. A shock wave induced by the ion beam in xenon propagates to the narrow end of the tube and becomes planar due to the multiple reflections at the interface to the tungsten shell. An increase of pressure due to reflection of the shock wave on the tungsten interface can be clearly seen on the pressure distribution at $t = 500$ ns and $t = 1100$ ns. Note, that the axis of symmetry is playing the role of the rigid wall, and the process of interaction at the axis is equivalent to a reflection. The reflection at the axis of symmetry corresponds to the time $t = 850$ ns. Because of the converging axial symmetry, the shock wave is amplified near the axis. A planar shock front results from the propagation of the ion beam launched shock in the tapered tube at $t = 1300$ ns. According to the simulations a pressure of 180 kbar, a density of 6.5 g/cm^3, and a temperature of 2800 K can be achieved in a planar geometry using such target design. Propagation of a planar shock in a tapered tube can be treated analytically [Lan02].

As it was shown in Fig. 4.1, the ion beam considered above produces in solid xenon a pressure of about 40 kbar in the Bragg peak. Use of a low diameter tube allows to produce a planar shock front with a pressure of 80 kbar. Introduction of the proposed tapered tube target configuration makes it possible to create a planar shock front with a pressure of 180 kbar, which is almost five times higher than that in the bulk xenon sample.

The numerical simulations of the shock wave propagation in a tapered

tube were performed with the BIG-2 hydrodynamic code developed in Chernogolovka, Russia [For96]. Simulation of irregular wave reflection on a rigid interface was tested by the authors of the code [Bus93]. The good agreement between simulations and experimental results for such a problem justifies experimental verification of the presented target configuration.

4.2 Isochoric heating of matter with heavy ion beams

Intense beams of energetic heavy ions have the advantageous property to deposit their energy with good uniformity over an extended volume. For ion energies $E_\mathrm{i} \gtrsim 100\,\mathrm{MeV/u}$, the stopping power of most materials is known to an accuracy of a few percent and is insensitive to details of chemical structure of the stopping material. If a beam current density profile is measured confidently, the total deposited specific energy, ϵ, is known to an accuracy of a few percent. Having prepared a sample at some initial density ρ_0, and having ensured that this density remains practically unchanged, it only remains to measure one physical quantity to obtain a point for the caloric equation of state, since the specific energy ϵ is already defined. In this case any measured physical quantity is determined as a function of the well defined thermodynamic state.

The SIS-18 synchrotron at GSI Darmstadt is able to provide intense beams of energetic heavy ions. Up to 2×10^{11} ions of U^{28+} accelerated to 200 MeV/u will be available in the near future [Spi99]. When focused on a spot with a radius of $\lesssim 0.5\,\mathrm{mm}$ (standard deviation of the Gaussian distribution), this ion beam will provide – for example in hydrogen – an energy deposition of $\epsilon \gtrsim 100\,\mathrm{kJ/g}$ (1 eV/atom). Hydrodynamic consistency between the deposited energy and the focal spot radius sets a limit on the pulse duration for the ion beam.

Hydrodynamic expansion of the heated sample, which should be minimized for quasi-isochoric experiments, is sensitive to the spatial profile of the ion beam current. For a rectangular radial profile, the density in the target center begins to drop only after the heating time $t_\mathrm{H} = r_\mathrm{b}/c(t)$ (r_b is the focal spot radius, and $c(t)$ is the sound speed), when the rarefaction wave reaches the axis of the target. Analytical calculations of the heating time and corresponding numerical simulations are presented in section 2.4. The perfomed calculations for the future SIS-18 ion beam show that the rarefaction wave arrives at the center of the target when the ion beam is still heating the target. However, a Gaussian current density profile would be more realistic. In this case, when the second spatial derivative of pressure is not zero, the density begins to drop in the vicinity of the target axis from the very start of the ion pulse. A typical example of this type of hydrodynamic motion

which can be solved analytically is the isentropic expansion of a sphere with a parabolic pressure profile [Zel67]. To keep the target density sufficiently constant during irradiation by a beam with the above parameters, a pulse duration below 20 ns is needed. According to the current plans, SIS-18 will not deliver beam bunches shorter than 100 ns.

Solid hydrogen was chosen as target material to illustrate the methods of quasi-isochoric heating of matter with heavy ion beams. Properties of hydrogen under extreme conditions are of great importance for astrophysics, inertial fusion applications and the problem of hydrogen metallization. In addition, solid hydrogen, as a low-Z material, allows a wide range of diagnostics possibilities, including powerful x-ray scattering technique [Nar98],[Gre03]. At GSI, the required pulsed x-ray source can be powered by the kilojoule PHELIX laser (providing a ns time resolution).

Heated quasi-isochorically with the SIS-18 ion beam, solid hydrogen will reach a temperature of about 1 eV, which corresponds to the regime of warm dense matter (WDM) [Lee00]. Warm dense matter is the region in temperature and density which can neither be regarded as condensed matter, i.e. $T \approx 0$, nor be described by theories of weakly coupled plasmas. Since this region covers a wide parameter range between solids and plasmas, WDM studies are of great relevance. WDM can be found in the interior of planets, cool dense stars and all plasma production devices, which start from cold dense matter (e.g., z- and x-pinches, laser-solid matter interaction, heavy ion beam driven plasmas, capillaries, exploding wires). With increasing plasma coupling parameter (which is the ratio of the inter-atomic potential energy to the thermal energy) perturbation approaches used in standard plasma phase theories fail because of the lack of small expansion parameters. To develop new theoretical methods, which can describe strongly coupled plasmas as well as high temperature condensed matter, we must be able to probe these states of matter experimentally. Isochoric heating of a macroscopic sample in the WDM regime which can be investigated applying x-ray scattering diagnostics, allows conclusions on the electron density, temperature and ion-ion correlations. For hydrogen, the warm dense matter parameter region is roughly $\rho = 10^{-3}$–1 g/cm^3, T = 0.1–20 eV.

Numerical simulations of the target hydrodynamics have been carried out with the two-dimensional hydrodynamics code BIG-2 [For96] supplemented by the SESAME equation of state tables [SES83]. The energy deposition of heavy ions was calculated using the SRIM code [Zie01]. Quasi-isochoric conditions along the beam axis are ensured by the ability of energetic heavy ion beams to heat matter nearly uniformly along the initial part of their trajectory, as long as the target is sufficiently long and expansion waves from the ends do not disturb the probed volume.

4.2.1 Ion beam parameters

The heavy ion synchrotron SIS-18 at GSI is able to deliver intense beams of energetic heavy ions suitable for creation of extended volumes of matter with high energy density. According to the accelerator parameters, the incoherent space charge limit allows acceleration of up to 2×10^{11} ions of U^{28+} to an energy 200 MeV/u, while several times 10^{10} particles can be reliably expected on target. Introduction of a powerful rf-buncher leads to a pulse compression that will provide pulses with a length of the order of 100 ns. To perform numerical calculations, we used a triangular temporal pulse power profile, which is close enough to the real beam shape. The spatial profile of the ion beam current is well approximated by a Gaussian distribution, $j \sim \exp(-r^2/2r_\mathrm{b}^2)$, where r_b is the focal spot radius. By employment of a quadrupole focusing system, the ion beams can be focused down to a spot radius of less than 0.5 mm. The beam energy of 200 MeV/u was chosen because it corresponds to the maximum magnetic rigidity limit of 18 Tm for the synchrotron. Lower energies are not desirable due to a reduced efficiency of the rf-buncher.

The governing parameter for proposed beam-matter interaction experiments is the specific energy deposition. For our analysis a specific energy of 130 kJ/g deposited in the center of the Gaussian beam distribution in a hydrogen sample was chosen. According to the SESAME equation of state, this corresponds to a temperature of about 0.6 eV in solid hydrogen, if the beam energy is fully converted into internal energy. A corresponding ion beam from SIS-18 would consist of 8×10^{10} uranium ions with an energy of 200 MeV/u focused on $r_\mathrm{b} = 350\,\mu$m.

4.2.2 Bare sample

The simplest target for quasi-isochoric experiments would be a bare sample of hydrogen, with a radius $R_\mathrm{H} \gtrsim r_\mathrm{b}$, if the density stays constant at least in part of the sample. For a rectangular spatial profile of the beam current, the density in the center of the irradiated region remains constant until the rarefaction wave arrives. However, for a Gaussian profile with a nonzero second spatial derivative of the pressure profile on the target axis the density begins to drop long before the rarefaction wave reaches the target center.

Figure 4.5 shows the density and temperature evolution in the center of a sample made of frozen hydrogen, during and shortly after irradiation by a Gaussian ion beam. Two cases are shown: in the first case the ion beam consists of 8×10^{10} particles, while in the second case the number of ions is increased by a factor of ten, and the focal spot radius is increased by $\sqrt{10}$ to keep the energy deposition equal to 130 kJ/g.

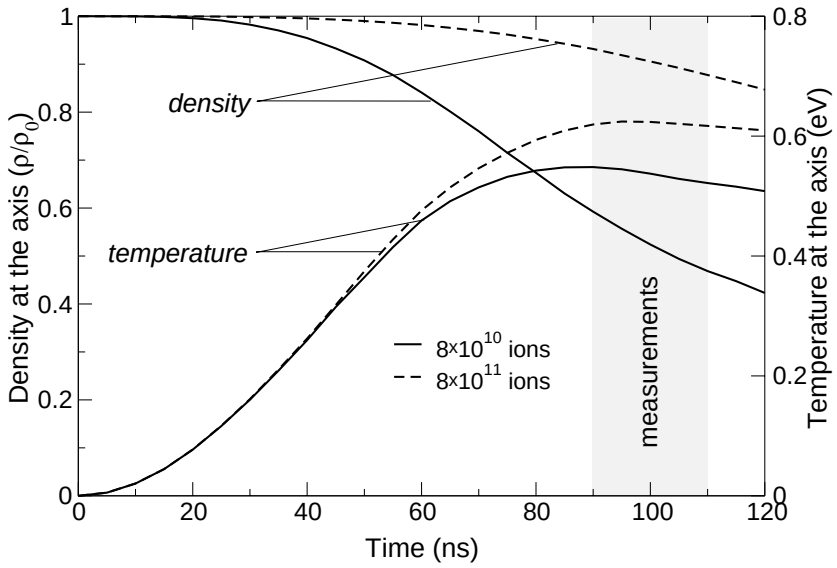

Figure 4.5: Evolution of density and temperature on the axis of a bare sample for 8×10^{10} and 8×10^{11} ions per pulse. The ion pulse length is 100 ns.

For 8×10^{10} ions, which is a realistic beam intensity for SIS-18, the density at the axis drops by a factor of two during the irradiation time, and the goal of quasi-isochoric heating is not reached. For the larger focal spot in the second case, which requires a higher number of ions, the density remains constant to a few percent, the temperature comes close to the maximum value of 0.64 eV. Hence, to heat a bare sample of matter quasi-isochorically by the SIS-18 ion beam, an intensity exceeding the incoherent space charge limit of the machine would be required.

4.2.3 Static confinement

With a limited number of ions, the adverse effects of the hydrodynamic expansion can be reduced by introducing an appropriate tamper, adjacent to the hydrogen. If the pressure in the heated sample remains below 100 kbar, quasi-isochoric conditions of beam irradiation can be provided by using a strong metal casing. In order to obtain homogeneous heating of the hydrogen in the radial direction, the heavy ion beam has to be collimated to use only the central part of the Gaussian distribution. The target consists of a stiff shell made of tungsten which contains frozen hydrogen. The inner part of the target is heated by the collimated beam (see Fig. 4.6). The hydrogen core has a radius of 100 μm.

Fig. 4.7 shows the radial profiles of density, temperature and sound speed in hydrogen after irradiation with the SIS-18 beam. According to the simulations, the hydrogen core expands only slightly, and the density remains constant to an accuracy of 10%. The temperature of about 0.6 eV ensures

that the conditions for quasi-isochoric heating are fulfilled. To obtain a point for the caloric equation of state, measurement of one physical quantity is sufficient. One possibility is to measure directly the pressure $p = p(\epsilon, \rho_0)$. However, a better and more practical alternative might be to measure the sound speed $c(\epsilon, \rho_0)$.

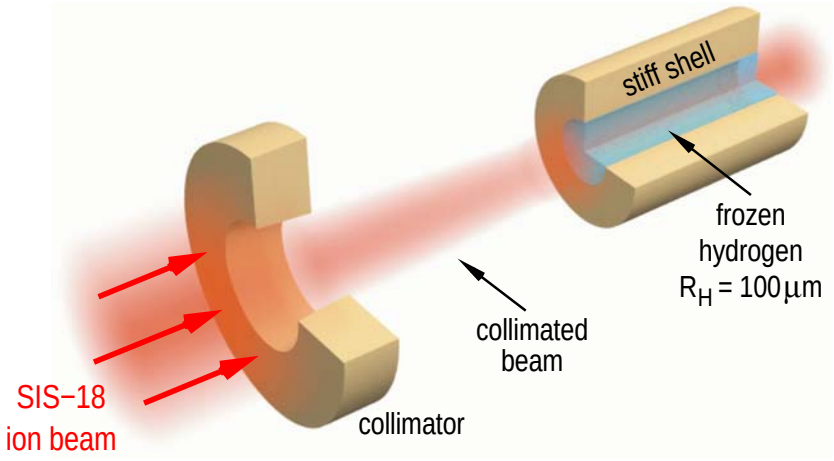

Figure 4.6: Target configuration for static confinement of frozen hydrogen. A stiff shell contains frozen hydrogen heated by the collimated SIS-18 ion beam.

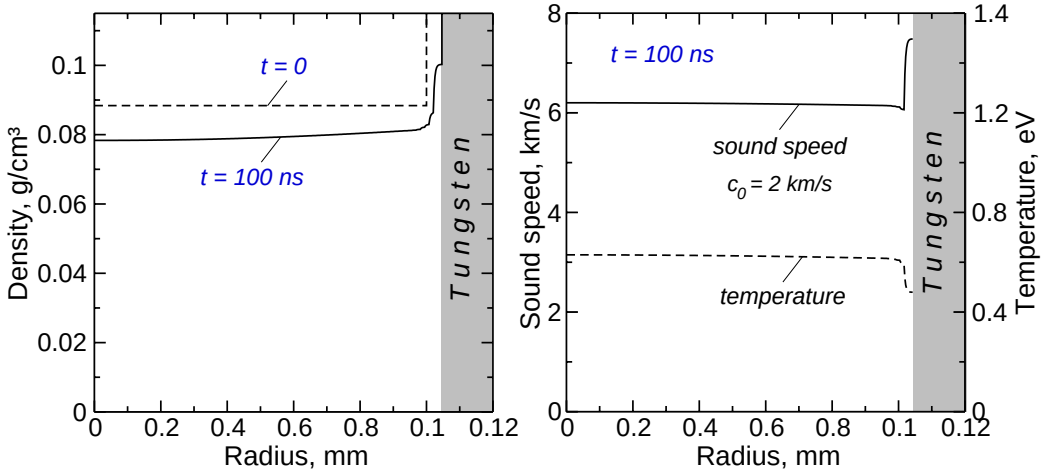

Figure 4.7: Radial distributions of density, temperature and sound speed in the hydrogen core for the target shown in Fig. 4.6, after irradiation by the collimated SIS-18 beam. The dashed line corresponds to the target density at $t = 0$. Initially frozen hydrogen has a sound speed of 2 km/s.

4.2.4 Dynamic confinement

The use of a massive, heavy-metal tamper to provide quasi-isochoric conditions of ion beam heating restricts the diagnostics possibilities. To apply powerful x-ray scattering diagnostics, the choice of target materials is limited to low-Z elements. To achieve confinement with a low-Z material, the tamper has to be heated by the wings of the ion beam in order to produce confining pressure on the main target material. A schematic view of the sample confined with a low-Z tamper is shown in Fig. 4.8.

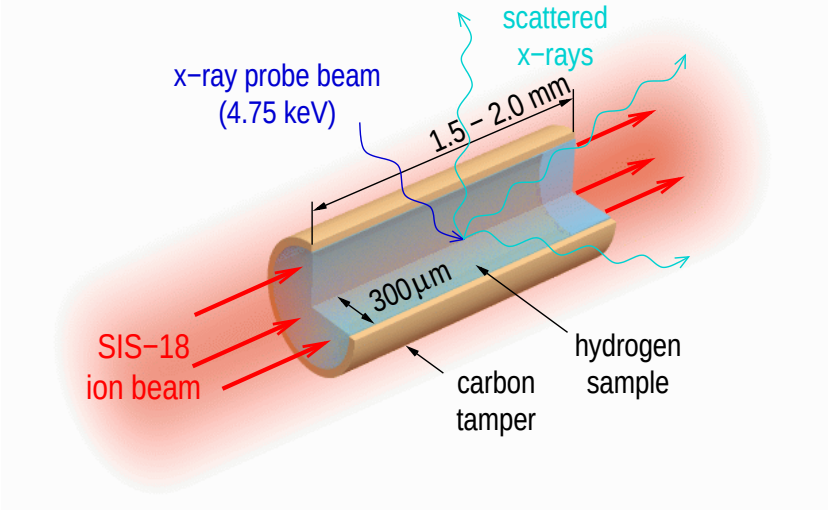

Figure 4.8: Target configuration for dynamic confinement of frozen hydrogen heated by the ion beam available from the SIS-18, and possible x-ray diagnostics.

Also, it is beneficial to use a tamper material with a large sublimation energy to delay the beginning of the hydrodynamic motion of the tamper. A carbon tamper would be a natural choice. First simulations have shown, however, that the tamper density should be lower than the normal density of graphite. As an appropriate substitute, the so called carbon phenolic was chosen. Carbon phenolic is a composite which is widely used in aerospace technology as a protective ablative material, made of about 70% carbon cloth which is bound by 30% of phenolic resin. According to the SESAME equation of state, it has a density of $1.5\,\mathrm{g/cm^3}$ at normal conditions. The radius of the hydrogen core R_H and the thickness of the carbon tamper $\triangle R_\mathrm{C}$ were optimized in numerical simulations. The smallest variations of the density of hydrogen were found for $R_\mathrm{H} = 300\,\mu\mathrm{m}$, $\triangle R_\mathrm{C} = 50\,\mu\mathrm{m}$.

The overall target behavior is shown in Fig. 4.9. During the ion pulse the carbon tamper expands outward from its initial thickness of $50\,\mu\mathrm{m}$ to a thickness of $220\,\mu\mathrm{m}$, and its density drops to about $0.3\,\mathrm{g/cm^3}$. At the same

time, the interface between the tamper and the hydrogen core moves only slightly, and the density of hydrogen remains almost constant except for a weak shock wave that is launched by the tamper at the beginning of the beam pulse. This shock wave is reflected from the target axis and arrives back at the tamper by the end of the ion pulse.

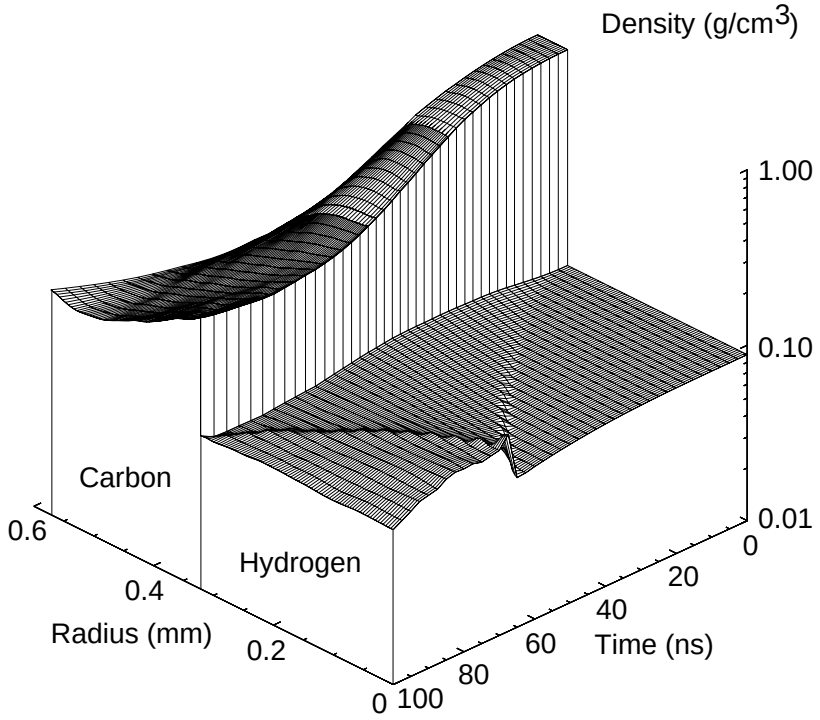

Figure 4.9: Density distribution vs radius and time for the target shown in Fig. 4.8, during the ion beam irradiation.

The quasi-isochoric heating of hydrogen is ensured by two competing processes: expansion of the hydrogen core and expansion of the carbon tamper. Initially, the hydrogen density begins to decrease on the target axis due to the Gaussian heating profile. At the same time, the pressure in the carbon tamper is higher than the pressure in the hydrogen core, and the C/H interface moves inward. Later on, as the density in the tamper drops, the pressure in the tamper decreases and the motion of the boundary comes to a halt. At still later times the increasing pressure in the core pushes the C/H interface back into its initial position.

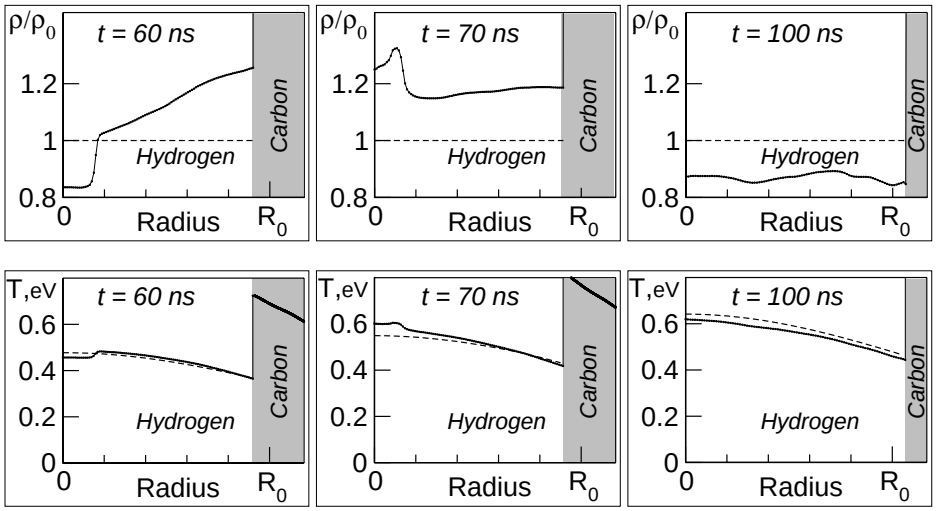

Figure 4.10: Radial density and temperature profiles in solid hydrogen confined with the low-Z tamper. The heavy ion beam consists of 8×10^{10} ions of U^{28+}. Solid lines correspond to a tamped sample, dashed lines illustrate the ideal isochoric heating.

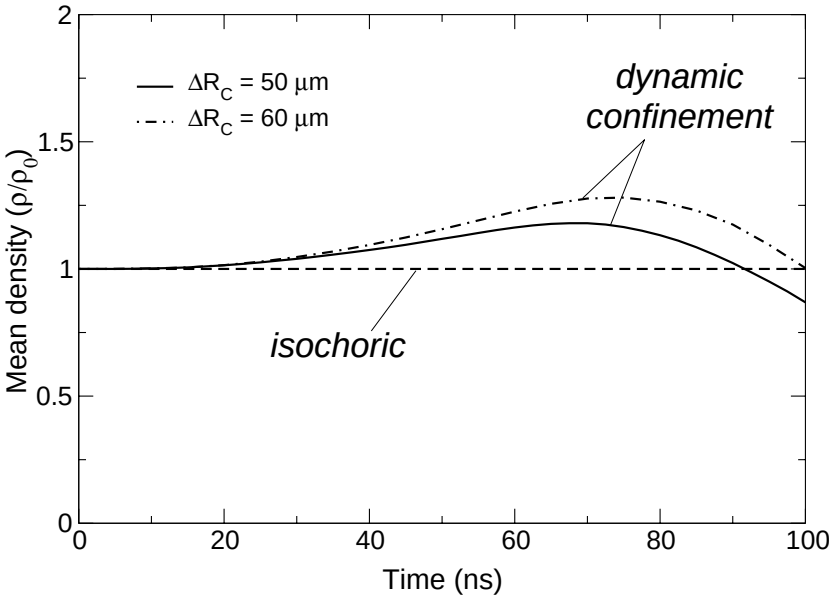

Figure 4.11: Evolution of the mean hydrogen density during the ion beam heating for two different thicknesses of the low-Z tamper.

Figure 4.10 shows the radial density and temperature profiles in hydrogen at different times. The solid lines relate to the target configuration shown in Fig. 4.8, while the dashed lines assume the ideal isochoric heating of frozen hydrogen by the same ion beam. At $t = 60\,\text{ns}$ the density near the axis is depressed, and the tamper moves inward and launches a weak shock wave.

At $t = 70\,\mathrm{ns}$ motion of the interface stalls, hydrogen is compressed by about 18%, and the reflected shock wave is running outward. At the end of the beam pulse, the density distribution along the radius is practically uniform, and differs by about 15% from the initial density of the frozen hydrogen. The temperature is ∼4% less than in the case of ideal isochoric heating.

In Fig. 4.11, the time evolution of the mean hydrogen density averaged over the radius is shown. The solid line corresponds to the thickness of the tamper of $50\,\mu\mathrm{m}$. In this configuration the smallest variations of the mean density during the beam heating were found. The dashed-dotted line is calculated for a $60\,\mu\mathrm{m}$ thick tamper. In this case the density of hydrogen after irradiation is equal to its initial value.

Notice, that the performed one-dimensional simulations also provide the necessary information required to estimate the target length. It is seen, that sound propagates twice the radius of the hydrogen core ($300\,\mu\mathrm{m}$) during the ion pulse. Hence, depending on the diagnostics requirements, the target has to be 1.5–2.0 mm long. Since the range of 200 MeV/u U ions in solid hydrogen is 45 mm, in carbon phenolic it is 6.4 mm, a good uniformity along the beam axis can be guaranteed.

4.2.5 Proposed diagnostics

The x-ray diagnostics is based on measuring the intensity, spectral and angular distributions of x-rays scattered by the heated sample. Providing valuable information on ion-ion correlations, electron and ion temperatures, x-ray scattering has the potential to become a powerful tool for investigations of warm dense matter. At high densities and relatively low temperatures, self-emission in the x-ray range is generally rather weak. If the level of this radiation is too low to be observed experimentally, we have to probe the sample with external x-rays. Due to the small scattering cross sections, high intensity x-ray sources are required. Such backlighter sources can be realized with the kilojoule PHELIX-laser beam at GSI [PHE98], e.g. using the thermally induced He-α x-ray emission of a mid-Z target element (e.g. Ti (E = 4.85 keV), Fe (E = 6.6 keV)) irradiated with ns-pulses or the hot electron induced hard x-ray K-α emission generated with very short laser pulses (1 ps, several 100 J).

X-ray scattering diagnostics can be used in two different modes. Spectrally unresolved scattering provides information about the ion-ion correlation by scanning the scattering angle. A spectrally resolved diagnostics, using a near backscattering geometry (scattering angle close to 180°), will allow the direct measurement of the electron density and temperature of the probed sample. Two aspects for the interpretation of the scattering data are important: the probing x-rays should suffer only small absorption in the sample, and the radial density profile should be homogeneous to provide scattering

from a volume of uniform density. As it is shown in Fig. 4.9, the radial density distribution is quite homogeneous after about 100 ns of heating and, therefore, well suited. Moreover, the low-Z tamper does not lead to strong absorption of the probe beam.

If the wavelength of the incident field, λ, is much smaller than the Debye length, $\lambda \ll \lambda_{\mathrm{D}}$, the wave interacts with the charges on a scale length in which they appear to be free. The scattering is obtained from the randomly distributed electrons, i.e., incoherent scattering. When the scattering wavelength is comparable to or greater than the Debye length, the incident wave interacts with shielded charges, i.e., one has coherent scattering. In addition, various types of electron and ion plasma waves propagate in plasmas even in thermodynamic equilibrium. Furthermore, in unstable situations enhanced periodic density fluctuations occur, and these can lead to a considerable enhancement of the level of coherent scattered power in the direction that satisfies momentum conservation for scattering from the particular plasma fluctuation. Both collective and non-collective spectrally resolved scattering regimes are accessible depending on scattering angles or tuning the x-ray energy using different backlighter target elements. With that, a wide range of scattering data can be provided for the investigation of warm dense matter [She75].

Chapter 5

Conclusions and outlook

It was the aim of this work to assess the possibilities of heavy ion beam heating of matter for equation of state studies. The considered ion beam parameters were limited to the capabilities of the SIS-18 synchrotron at GSI. In chapter four it was shown, that relevant experiments can be performed in the near future to measure EOS data in the warm dense matter regime. As an example, the dynamic confinement of a solid hydrogen target was proposed providing the possibility of x-ray scattering diagnostics, which reveals information on electron temperature and density, and on ion-ion correlations.

An intense x-ray source is needed to apply the x-ray scattering diagnostics, because the scattering cross section is extremely small. Samples of matter heated uniformly with heavy ion beams using a dynamic confinement scheme are large and dense, and therefore perfectly suited for the x-ray scattering technique. The choice of the target material was primarily dictated by the energy of the available x-ray line radiation. The dynamic confinement method can be extended to other materials, as long as it is possible to probe the heated volume. One can also use the method of dynamic confinement for higher beam intensities. The number of ions, pulse length, and beam focus should be consistent, so that the weak shock wave launched from the tamper into the confined material cannot return to the tamper before the end of the heating pulse. This process is determined by the sound speed in the confined material which increases with temperature and therefore with beam intensity.

To validate the hydrodynamic code that was used to calculate novel targets for future EOS measurements, an experimental investigation of intense heavy ion beam interaction with matter was performed. Two-dimensional time resolved schlieren imaging was applied to visualize the response of ion beam heated matter. To construct a schlieren image out of a hydrodynamic simulations, 3D ray-tracing modeling was carried out. Comparing computed and measured schlieren images allows to interpret the experimental data as well as to test the hydrodynamic code extensively. This has shown, that the

hydrodynamic calculations are sufficiently developed to describe the behavior of ion beam heated targets. The discrepancies between the experimental schlieren images can be related to the EOS data used in the hydro calculations. The important ability of the schlieren technique to detect phase boundaries in the target was found by analysis of the schlieren data. It was also shown, that for a target with high yield point, where hydrodynamic motion was not induced by the ion beam, the schlieren diagnostics can help to estimate the temperature in the heated region by detecting the thermal diffusion. An information on the target temperature was also obtained by analysis of irreversible changes in the target after irradiation.

A new target configuration for EOS measurements of shock compressed matter driven by SIS-18 ion beams was proposed in this work. It allows to create a planar shock wave out of initially inhomogeneous target loading with a pressure which is several times higher than in a bulk sample. However, the intense heavy ion beams cannot compete with conventional drivers for shock wave experiments, like high-power lasers, high explosives, or Z-pinch machines. To perform EOS measurements in interesting regions of the phase diagram, the property of ion beams to heat an extended volume of matter with good uniformity has to be utilized.

To perform the proposed EOS measurements based on x-ray scattering in dynamically confined targets several steps are necessary. First, the concept of dynamic confinement has to be demonstrated experimentally. To build the described target, the available cryogenic technology [Fun99] has to be improved to produce homogeneous solid hydrogen targets surrounded by a low-Z tamper. As a test of the target, x-ray backlighting of the hydrogen/tamper boundary can be performed. In parallel the powerful, but also very demanding x-ray scattering diagnostics has to be developed at GSI. Since the scattering cross sections are extremely small, it relies on the availability of an intense narrow band x-ray source and requires in addition the most efficient x-ray spectrometers that are available.

The investigation of matter at high energy density is a very active field of growing importance. This is reflected in the fact, that the most powerful drivers like the Z-machine in Sandia [San03] and the laser facilities in Livermore [NIF03] are currently upgraded, and new machines like the TESLA XFEL [Mat02] will enter the field. With the installation of the planned new accelerator facilities in Darmstadt and the unique possibility of volumetric heating, GSI can become a leading laboratory for high energy density research.

Bibliography

[Ahl80] S.P. Ahlen, Rev. Mod. Phys. **52**, 1(1980)

[Alt65] L.V. Altshuler, Sov. Phys. Usp. **8**, 52(1965)

[Arm72] B.H. Armstrong, R.W. Nicholls, "Emission, Apsorbtion and Transfer of Radiation in Heated Atmospheres", Pergamon, Oxford (1972)

[Arn87] R.C. Arnold and J. Meyer-ter-Vehn, Rep. Prog. Phys. **50**, 559(1987)

[Arn88] R.C Arnold and J. Meyer-ter-Vehn, Atoms, Molecules and Clusters **9**, 65(1988)

[Bas85] M. Basko, Sov. High Temperature **23**, 388(1985)

[Bic72] H. Bichsel, in A.I.P. Handbook, edited by D.E. Gray, McGraw–Hill, New York, pp. 8–142 (1972)

[Bet30] H.A. Bethe, Ann. Phys. **5**, 325(1930)

[Betz83] H.D. Betz, Applied Atomic Collision Physics, Academic Press, New York, Vol. IV, pp. 1–42 (1983)

[Blo33] F. Bloch, Ann. Physik **16**, 287(1933)

[Boh15] N. Bohr, Philos. Mag. **30**, 581(1915)

[Bor02] M. Born and E. Wolf, "Principles of Optics", 7th edition, Cambridge, University Press (2002)

[Bus87] A.V. Bushman and V.E. Fortov, Sov. Tech. Rev. B. Therm. Phys. **1**, 219(1987)

[Bus93] A.V. Bushman, G.I. Kanel, A.L. Ni, V.E. Fortov, "Intense dynamic loading of condensed matter", Tailor & Francis (1993)

[Con02] C. Constantin, PhD thesis: "Multiple weak shock waves induced by heavy ion beams in solid matter", Universität Darmstadt (2002)

[Cou99] R. Courant, K.O. Friedrichs, "Supersonic flow and shock waves", Springer (1999)

[Die92] K.-G. Dietrich, D.H.H. Hoffmann, E. Boggasch, J. Jacoby, H. Wahl, M. Elfers, C.R. Haas, V.P. Dubenkov, A.A. Golubev, Phys. Rev. Lett. **69**, 3623(1992).

[Dew03] E. Dewald, C. Constantin, C. Niemann, S. Udrea, J. Jacoby, J. Wieser, D. Varentsov, N.A. Tahir, A. Kozyreva, A. Shutov, T. Schlegel, A. Tauschwitz, D.H.H. Hoffmann, and R. Bock, IEEE Transactions on Plasma Science **31**, 221(2003)

[Efr94] V. Efremov, PhD thesis: "Investigation of intense pulse actions under composites materials", Institute for High Temperatures, Moscow (1994)

[Eid00] K. Eidmann, J. Meyer-ter-Vehn, T. Schlegel, S. Hüller, Phys. Rev. E **62**, 1202(2000)

[Eli02] S. Eliezer, A. Ghatak, H. Hora, "Fundamentals of Equations of State", World Scientific Publishing, Singapore (2002)

[Emr81] Ed. R.J. Emrich, "Methods of Experimental Physics" vol. 18A, Academic Press (1981)

[Fan63] U. Fano, Ann. Rev. Nucl. Sci. **13**, 1(1963)

[For96] V.E. Fortov, B. Goel, C.-D. Munz, A.L. Ni, A.V. Shutov, O.Yu. Vorobiev, Nucl. Sci. Eng. **123**, 169(1996)

[Fun99] U.N. Funk, Dissertation: "Aufbau und erster Einsatz einer Kryoanlage zur Herstellung von Wasserstofftargets für Experimente mit Schwerionenstrahlen", Universität Erlangen-Nürnberg (1999)

[Gra93] R.A. Graham, "Solids under high-pressure shock compression", Springer (1993)

[Gre03] G. Gregori, S.H. Glenzer, W. Rozmus et al., Phys. Rev. E **67**, 026412(2003)

[Gut01] H.H. Gutbrod, K.D. Groß, W.F. Henning, V. Metag (Eds.) "An International Accelerator Facility for Beams of Ions and Antiprotons", GSI Darmstadt (2001)

[Hof94] D.H.H. Hoffmann, J. Jacoby, W. Laux, M. de Magistris, E. Boggasch, P. Spiller, C. Stöckl, A. Tauschwitz, K. Weyrich, M. Chabot, and D. Gardes, Nucl. Instr. Meth. B **90**, 1(1994)

[Ims86] V.S. Imshennik, I.N. Mikhailov, M.M. Basko, S.V. Molodtsov, Sov. Phys. – JETP **63**, 980(1986)

[Jac75] J.D. Jackson, "Classical Electrodynamics", 2nd edition, Wiley, New York (1975)

[Koz03] A. Kozyreva, M. Basko, F. Rosmej, T. Schlegel, A. Tauschwitz, and D.H.H. Hoffmann, accepted for publication in Phys. Rev. E

[Lan02] L.D. Landau, E.M. Lifshitz, "Fluid Mechanics", 2nd edition, Butterworth-Heinemann (2002)

[Lar59] A.I. Larkin, JETP **37**, 264(1959)

[Lee00] R.W. Lee et al., Science at the LCLS: Plasma based studies, preprint (2000)

[Len00] T.J. Lenosky, et al., Phys. Rev. E **61**, 1(2000)

[Lin61] J. Lindhard, M. Scharff, Phys. Rev. **124**, 128(1961)

[Lin96] J. Lindhard, A.H. Sørensen, Phys. Rev. A **53**, 2443(1996)

[Mal65] I.H. Malitson, J. Opt. Soc. Am. **55**, 1205(1965)

[Mao94] H.K. Mao and R.J. Hemley, Rev. Mod. Phys. **66**, 671(1994)

[Mar80] S.P. Marsh (Ed.), "LASL Shock Hugoniot Data", Univ. of California Press, Berkeley–Los Angeles–London (1980)

[Mat02] G. Materlik and Th. Tschentscher (Eds.), "TESLA Technical Design Report", Part V, DESY, Hamburg (2002), see also <http://tesla.desy.de/>

[Nar98] E. Nardi, Z. Zinamon, D. Riley et al., Phys. Rev. E **57**, 4693(1998)

[NIF03] "National Ignition Facility Programs", available from <http://www.llnl.gov/nif/>

[PHE98] PHELIX Petawatt High-Energy Laser for Heavy Ion Experiments, GSI Report **98-10**, 12(1998)

[Ren88] R.J. Renka, ACM Transactions on Mathematical Software **14**, 139(1988)

[San03] "Z-Machine", available from <http://zpinch.sandia.gov>

[SES83] SESAME'83: Report on the Los Alamos Equation-of-State Library, T4-Group, Los Alamos National Laboratory Report No. LALP-83-4, Los Alamos 1983

[Set01] G.S. Settles, "Schlieren and Shadowgraph Techniques", Springer (2001)

[Sch90] P. Schiebener, J. Straub, J.M.H. Levelt Sengers and J.S. Gallagher, J. Phys. Chem. Ref. Data **19**, 677(1990)

[She75] J. Sheffield, "Plasma Scattering of Electromagnetic Radiation", Academic Press, New York (1975)

[Spi99] P. Spiller et al., Proc. of the PAC 99, 1788(1999)

[Sta60] K.P. Stanyukovich, "Unsteady Motion of Continuous Media" (M. Holt, ed.), Academic Press, New York (1960)

[Rag84] Charles E. Ragan III, Phys. Rev. A **29**, 1391(1984)

[Ros65] D. J. Rose, J. M. Clark, "Plasmas and Controlled Fusion", M.I.T. Press, Massachusetts (1965)

[Rot00] M. Roth, C. Stöckl, W. Süss, O. Iwase, D.O. Gericke, R. Bock, D.H.H. Hoffmann, M. Geissel and W. Seelig, Europhys. Lett. **50**, 28(2000).

[Zel67] Ya.Z. Zeldovich, Yu.P. Raizer, "Physics of Shock Waves and High-Temperature Hydrodynamic Phenomena", Academic Press, London (1967)

[Zie85] J.F. Ziegler, J.P. Biersack, U. Littmark, "The Stopping and Range of Ions in Solids" Vol. 1, Pergamon Press, New York (1985)

[Zie01] J.F. Ziegler, J.P. Biersack, computer program SRIM-2000/01. Available from <http://www.srim.org>

Acknowledgements

I am grateful to people whose contributions made my PhD thesis possible and who helped me to overcome all the difficulties over the last years. In particular I would like to thank:

Prof. Dr. Dr.h.c. Dieter H.H. Hoffmann who offered me the opportunity to work on an interesting subject of research, for his continuous support and interest in the results.
Hessische Ministerin für Wissenschaft und Kunst for the financial support (HWP-Programm).
Dr. Theo Schlegel for the thorough supervising of the theoretical part of the work. He was always open for questions and discussions.
Prof. Mikhail Basko for much time he patiently spent teaching me a profound knowledge of physics and for offering many helpful suggestions.
Dr. Andreas Tauschwitz and Prof. Joachim Jacoby for strong support in the experimental part of the work.
Dr. Frank Rosmej for the incentive to work on a dynamically confined target.
Dr. Vladimir Efremov for many discussions and advice in preparing and interpretation of the experiment.
Alexander Shutov for his help in running the hydrodynamic code BIG-2.
Prof. Jürgen Meyer-ter-Vehn for fruitful and open discussions.
Dr. Jochen Wieser, Serban Udrea, Udo Geißler, Petra Schwab for their assistance during the beamtime and beamtime preparations.
Dr. Dobre Dobrev for his help with the electron microscopy of the fused silica targets.
Horst Balonier, Dr. Abel Blazevic, Erik Brambrink, Dr. Carmen Constantin, Dr. Eduard Dewald, Dr. Ulrich Funk, Dr. Matthias Geißel, Renate Knobloch, Stephan Neff, Dr. Christoph Niemann, Viktorija Oršić Muthig, Dr. Olga Rosmej, Prof. Markus Roth, Dr. Peter Spiller, Heinrich Wahl, Dr. Karin Weyrich for their support.
Prof. Joachim Jacoby, Renate Knobloch, Dr. Theo Schlegel, Dr. Andreas Tauschwitz for corrections of the manuscript.
Bibliothek, Targetlabor, and Werkstatt at GSI for excellent technical support.

Curriculum Vitae

Name:	Anna Kozyreva
Birth date / place:	December 16, 1975 / St.-Petersburg, Russia
Citizenship:	Russian

Educational profile:

since Sept. 1999	PhD student at the Technical University, Darmstadt and at Gesellschaft für Schwerionenforschung, Darmstadt, Germany Promotionsstipendium from Hessische Ministerin für Wissenschaft und Kunst (HWP-Programm)
1992-1998	Bachelor of Physics / Master of Physics at the Saint-Petersburg State Technical University, Russia Specialization: Optical Physics and Quantum Electronics Master's thesis: "Numerical Modeling of Stochastic NMR Experiment" Diploma with honors
1990-1992	High-School for Mathematics and Physics, St.-Petersburg
1982-1990	Primary and secondary school, St.-Petersburg